land

Article

Back Analysis of a Real Debris Flow, the Morino-Rendinara Test Case (Italy), Using RAMMS Software

Antonio Pasculli [1,2], Claudia Zito [1], Nicola Sciarra [3,*] and Massimo Mangifesta [3]

[1] Department of Engineering and Geology, University "G. d'Annunzio" of Chieti-Pescara, Via dei Vestini, 31, 66100 Chieti, Italy; antonio.pasculli@unich.it (A.P.); claudia.zito@unich.it (C.Z.)
[2] INDAM Research Group GNCS, National Group of Scientific Computing, National Institute of Advanced Mathematics, University "G. d'Annunzio" of Chieti-Pescara, 66100 Chieti, Italy
[3] Department of Science, University "G. d'Annunzio" of Chieti-Pescara, Via dei Vestini, 31, 66100 Chieti, Italy; mmangifesta@unich.it
* Correspondence: nicola.sciarra@unich.it

Abstract: Debris flows are a dynamic and hazardous geological phenomenon, as by definition, debris flows are rapid, gravity-driven flows of saturated materials that often contain a mixture of water, rock, soil, and organic matter. They are highly destructive and occur in steep channels, posing a significant threat to infrastructure and human life. The dynamics of debris flows are complex due to their non-Newtonian behaviour and varying sediment–water interactions, making accurate modelling essential for risk mitigation and emergency planning. This paper reports and discusses the results of numerical simulations of back analyses aimed at studying the reconstruction of a real rapid debris flow. The selected test case is the event that occurred on 12 and 16 March 2021 along the Rio Sonno channel, a tributary of the Liri River, following the landslide event of Rendinara (Municipality of Morino, Abruzzo Region, Italy). There are significant flow sources in the area, fed by a highly fractured carbonaceous aquifer that extends immediately upslope of the detachment zone. The continuous flow influences the saturation level in the fine-grained sediments and favours the triggering of the debris flow. This phenomenon was simulated using the commercial RAMMS code, and the rheological model selected was "Voellmy fluid friction". The modelling approaches used in this research are valid tools to estimate the volumes of materials involved in the flow-feeding process and for the purpose of possible mitigation works (debris flow-type dams, weirs, flow diversion, etc.).

Keywords: rapid debris flow; numerical simulations; FEM; rheological models; RAMMS software

check for updates

Citation: Pasculli, A.; Zito, C.; Sciarra, N.; Mangifesta, M. Back Analysis of a Real Debris Flow, the Morino-Rendinara Test Case (Italy), Using RAMMS Software. *Land* **2024**, *13*, 2078. https://doi.org/10.3390/land13122078

Academic Editor: Fabrizio Terenzio Gizzi

Received: 9 October 2024
Revised: 27 November 2024
Accepted: 28 November 2024
Published: 3 December 2024

Copyright: © 2024 by the authors. Licensee MDPI, Basel, Switzerland. This article is an open access article distributed under the terms and conditions of the Creative Commons Attribution (CC BY) license (https://creativecommons.org/licenses/by/4.0/).

1. Introduction

In the context of natural hazards, as it is well known, there is a growing need for process models to predict both the velocities and the volumes of complex landslides.

This increase in landslide research is driven by several factors, including climate change [1], which has intensified the frequency and severity of extreme weather events, leading to more frequent landslides [2]. Urbanisation and land-use changes further exacerbate these risks by destabilising slopes and altering natural drainage patterns [3]. As populations continue to grow in vulnerable areas, understanding the mechanics of landslides becomes crucial for mitigating their impacts and enhancing community resilience [4]. Such models are particularly useful for the development of mitigation measures, such as embankments and rockfall barriers [5], or also to predict obstructions in rivers that could cause overflows. Hazard mapping is a particularly important need in all areas affected by similar events [6]. The accurate prediction of runoff distances, flow velocities, and impact pressures is the main motivator for the development of dynamic mass movement models. Accordingly, mathematical and numerical approaches have been proposed, some of the most common of which will be summarised in the subsequent sections for the sake of

completeness. However, a fundamental problem for the application of any mathematical–numerical model is the selection of the values of the physical, hydrological, geomechanical, etc., parameters required for the closure of the equations [7].

In addition to process models, there are various methods for obtaining parameters that can be integrated into these models. Remote sensing technologies, such as satellite imagery and aerial photography, facilitate large-scale assessments of land stability by detecting changes in vegetation, soil moisture, and surface displacement. These data are essential for improving the accuracy of numerical models, as they provide critical information on the initial conditions and ongoing changes in the landscape that may influence landslide behaviour.

Geographical Information Systems (GISs) play a pivotal role in integrating diverse data sources, including geological, hydrological, and topographical information, to develop comprehensive numerical models. By employing GISs, researchers can visualise spatial relationships and quantify the risk factors associated with landslide susceptibility, which can then be incorporated into the modelling process to improve predictions of landslide occurrences and dynamics [8].

Ground-based techniques, such as in situ measurements and monitoring systems, offer real-time data on slope stability and hydrological conditions. This information is vital for calibrating numerical models, as it allows for the validation of model predictions against actual field conditions [9]. Furthermore, integrating ground-based data helps to refine the physical and geomechanical parameters used in the models, ensuring that they accurately reflect the complexities of the terrain.

These complementary approaches enhance the predictive capabilities of numerical models in landslide research and enable more effective risk management strategies. By combining remote sensing, GISs, and ground-based techniques, we can create robust models that not only simulate landslide phenomena but also inform decision-making processes aimed at mitigating risks to communities and infrastructure.

Therefore, the main purpose of this article is to calibrate and estimate, in backfitting mode, the numerical values of some of the parameters required for the application of suitable software to a real study case. In this work, RAMMS v1.5 software (Rapid Mass Movement Simulation, [10–17]) was used. The computer code is based on the Finite Element Method (FEM), and we used it to calculate the rapid mass movement evolution. Moreover, the use of the Shallow-Water approach, as implemented in RAMMS, allows a 2D model to be applied to 3D problems through a process of "averaging" the flow along the third dimension, assumed to be negligible compared to the others, with velocities parallel to the topographic surface. The flow is described using a Eulerian approach. The code is coupled with a user-friendly visualisation tool that allows the simulation results to be easily accessed, visualised, and analysed. The Voellmy–Bartelt rheological model has been developed and implemented in RAMMS through calibration and verification in full-scale trials at sites such as the Vallée de la Sionne (Switzerland). The RAMMS code was applied to study the Morino-Rendinara landslide (Figure 1). This type of landslide is classifiable as a fast flow (debris flow) and must be studied in the context of the complex geological evolution of the entire Roveto Valley, which is crossed, for approximately 30 km, by the Liri River.

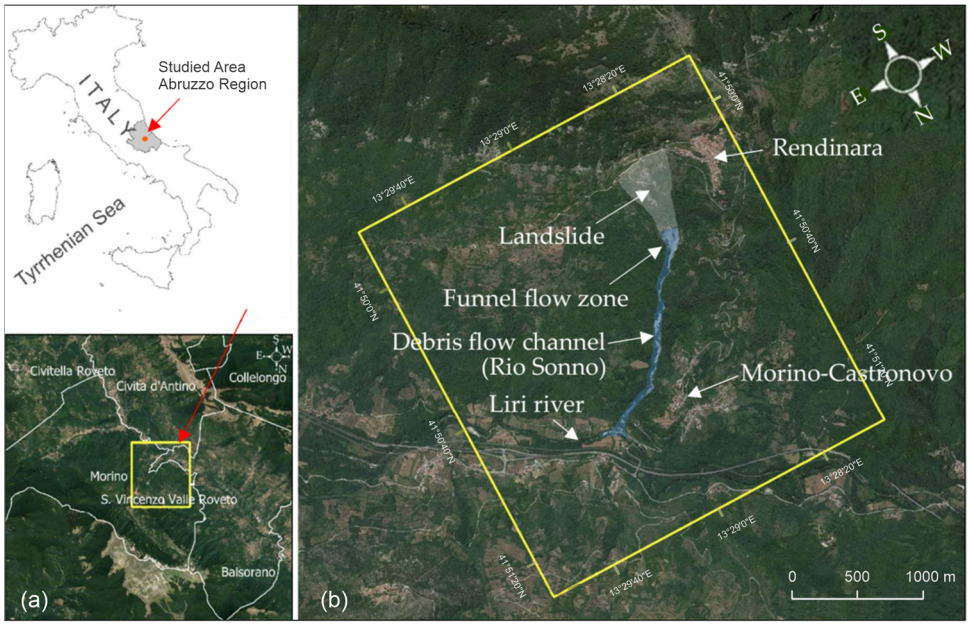


Figure 1. (**a**) The Roveto Valley located in the Abruzzo Region (Italy); (**b**) zoomed-in map of the landslide extension in the Rio Sonno/Fiume Liri area.

2. Study Area Overview

Rendinara is a small hamlet in the Municipality of Morino in central Italy (Abruzzo Region). The area is in the upper part of the Roveto Valley, near the border of the Abruzzo and Lazio Apennines (Figure 1a), on the eastern side of the Liri River valley. The Roveto valley is mainly characterised by Messinian siliciclastic deposits, with secondary occurrences of polygenic breccias and puddings. These formations are represented by fractured carbonate rocks that tectonically overlie Messinian sandstone–schist formations. The accentuated fracturing has led to the accumulation of slope debris, on which of Rendinara hamlet is located. In additional, this slope has been deeply incised by meteoric erosion. Within the study area, numerous high-flow springs derive their water supply from a highly fractured carbonate aquifer. The area under study is affected by a large landslide phenomenon with a maximum length of about 900 m at its head at an altitude of about 850 m a.s.l. The hamlet of Rendinara is lapped by the landslide crown throughout its extension. The landslide develops in a north-easterly direction towards the Liri River valley.

The area is affected by various types of movements that are characterised by wall collapses consisting of Mesozoic carbonate rocks located on direct faults [18–24]. These walls are outside the crown area, but the detritus produced by these collapses goes to supply the summit part of the landslide body, where numerous steps, trenches, and recent counter-slopes can be observed, testifying to the presence of an active movement in correspondence with mostly detrital material. Therefore, the landslide can be distinguished into two areas: starting from the summit at 850 m a.s.l. up to an elevation of approximately 630 m, there is the feeding basin of the flow (Figure 1b, grey area), which, due to the geological conformation of the site, assumes a triangular shape until it closes in a funnel shape on the impluvium that regulates the flow of the Rio Sonno (Figure 1b, blue area). Below this elevation, the landslide evolves as a channelled flow until it reaches the Liri River at an elevation of approximately 403 m. In the funnel area, surface runoff and groundwater have generated an important landslide scarp that also highlights the presence of high-flow springs. The springs, which are certainly numerous in the area, are set at the boundary between fractured carbonate formations and clay formations in tectonic contact, as shown in Figure 2. Figures 3 and 4 show the profile of the entire flow path, with the relative heights and dimensions.

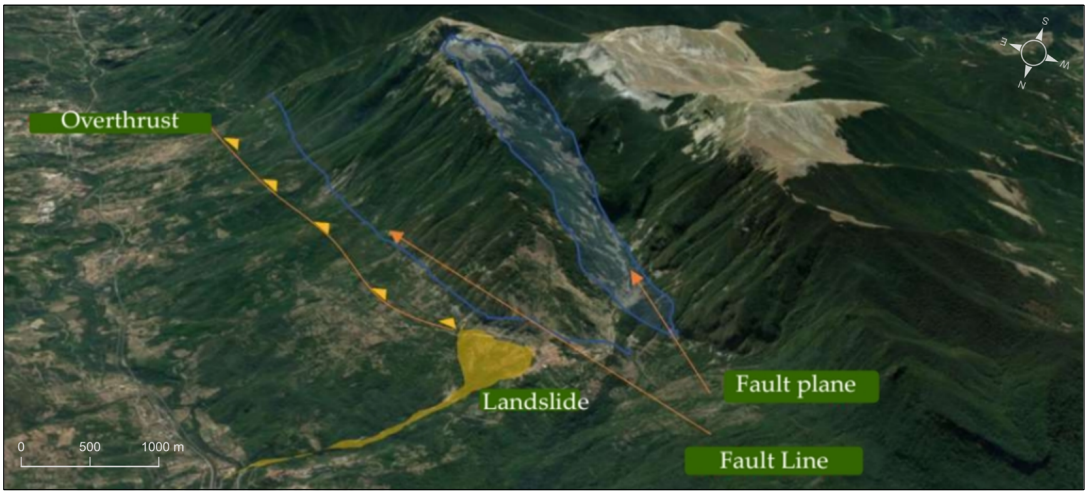


Figure 2. Schematisation of tectonic lineament map.

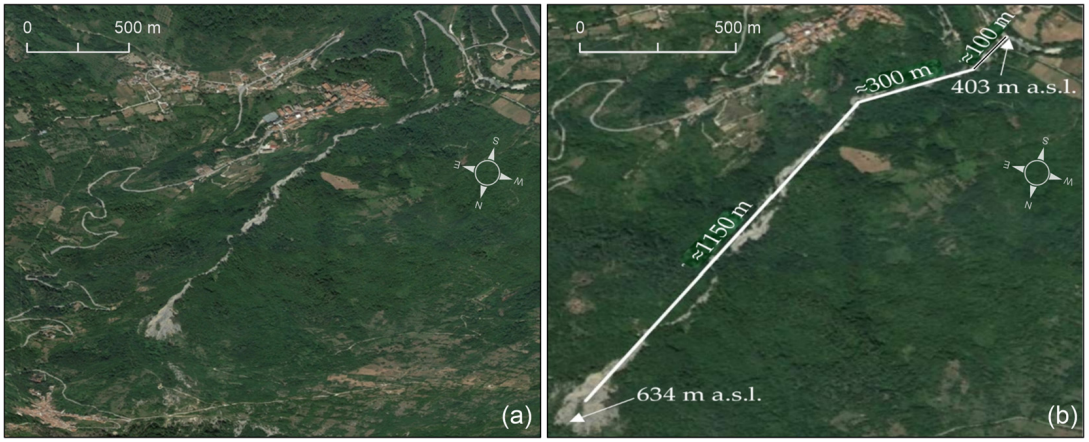


Figure 3. (**a**) Photo of the debris flow channel planimetry (Google Earth imagery); (**b**) longitudinal dimensions of the channel with the elevation.

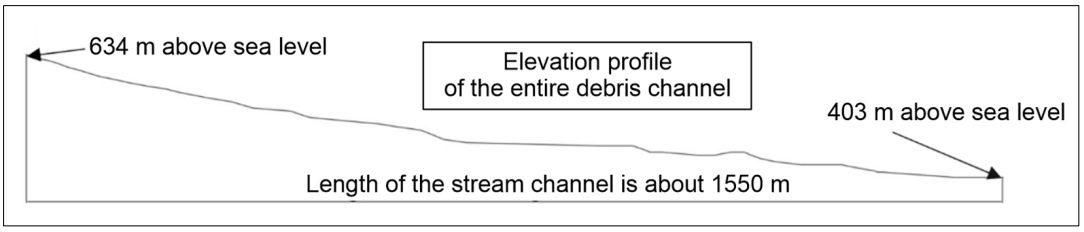


Figure 4. Sketch of the channel profile with the projected dimensions.

The landslide materials, according to the local geology, consist mainly of boulders and carbonate debris in an abundant clay matrix. Figure 5 shows photos of the area, taken with a drone, while Figure 6 shows photos of the solid material deposited at the confluence between the Rio Sonno and the Liri River and a zoomed-in image of the bridge over the Liri River. The photos were taken during the geological survey immediately after the conclusion of the event. The height of the material deposited in those areas is one of the main parameters taken into consideration to carry out the parametric analyses for backfitting.



Figure 5. Photos of some areas of the debris stream channel (Rio Sonno). (**a**) The upper part of the debris stream channel. (**b**) Zoomed-in photo of the selected area in Figure 5a. (**c**) The lower part of the debris stream channel.

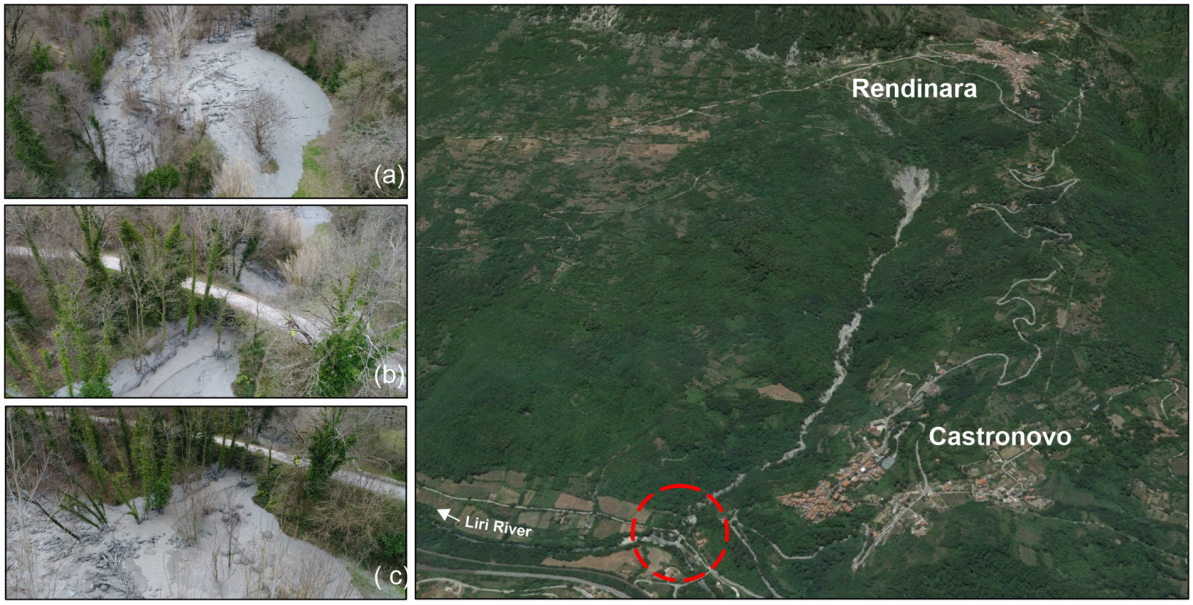


Figure 6. (**a**–**c**): Bridge near the Liri River near the confluence of the Rio Sonno, along which the debris was channelled (red circle).

The phenomenon that occurred was governed by the presence of an irregular and heterogeneous mass of sediments upstream, inland waters of considerable flow, and high slope gradients (in some places even 45%). The heterogeneity of the material covering the entire study area and the presence of large quantities of water from the fractured carbonate aquifer contribute to instability, particularly due to fluctuations in the water table that are associated with the local climate and rainfall patterns. These fluctuations can weaken the mechanical properties of the cover layer, increasing instability and feeding the debris flow source zone. The triggering mechanism was identified in the filtration motion and in the formation of transient flows of water, flowing through unstable sedimentary deposits, as just suggested in another study on the area [17,25]. Among the simplest methods for establishing the critical conditions necessary for triggering an earth flow are those based on the duration and intensity of rainfall (or even snowmelt), although they have the defect of being adoptable only in the geomorphological contexts in which they were originally derived. Moreover, as in our case, the flows may cause further damage when the final deposition occurs on the riverbed in the valley bottom, blocking its section and forcing it to overflow its banks, causing problems to nearby houses and infrastructures.

3. Materials and Methods

Below is a brief presentation, in the form of a "Flow Chart", of the structure of the chapter and the approaches selected to carry out the simulations that are discussed in the subsequent chapters. Section 3.1, "Model Description", introduces the general characteristics of the selected model, the "Shallow-Water" approach, and the Voellmy model, as the rheological constitutive equation, included in RAMMS software. Then, in Section 3.2, "Selected Mathematical–Numerical Model", a summary of the most common techniques and constitutive equations proposed in the literature was given, divided into methods that require the tessellation of the domain by means of geometric elements (2D or 3D) and methods that do not require the discretisation of the continuum. Therefore, a brief discussion of their advantages and disadvantages has also been added in Sections 3.2.1–3.2.3 in order to make the article as self-consistent as possible. Section 3.3, Channel Curvature, describes the model that also considers the curvature of the debris flow pathway. Finally, Section 3.4, Numerical Models, with its associated sub-sections, provides a concise description of the numerical final stage topics in the construction of a computational model. This section describes a numerical approach that does not require the discretisation of the continuum (meshless approach) and the method adopted by RAMMS, which, instead, is based on the tessellation of the continuum through simple geometric elements (i.e., triangles).

3.1. Model Description

In the following section, the setup of the model will be explained, starting with the governing equations of the phenomenon, which are described by mathematical and numerical models. In this case, Shallow-Water Equations (SWEs) are the most suitable, as they provide a simplified and computationally efficient representation of mass flows over large areas, capturing the essential dynamics of the flow and its interaction with the terrain without the need for highly detailed simulations. This will be followed by an explanation of the dynamic behaviour of the constituent materials using rheological model equations, specifically represented using the Voellmy model. This model offers a realistic representation of frictional forces and efficiently handles high-speed, high-energy flows.

Due to the complexity and significant influence of water in the landslide system, a dedicated section will describe the erosion parameters. These parameters are crucial because of the low cohesion of the materials covering the slope, the substantial water input from the upper carbonate aquifer, and the high-flow springs along the slope. Finally, the channel curvature will be considered due to the natural variation of the channel, which causes changes in centrifugal forces, affecting both the velocity and flow height.

3.2. Selected Mathematical–Numerical Model

The most general and "ab initio" commonly exploited approach focused on studying material flow is based on the Balance Equations of physics, pursued using Computational Fluid Dynamics (CFD). Namely, Navier–Stokes and Newton's laws' equations must be solved and supplemented with experimental laws that define the parameters related to the mass transport of the material, the rate of erosion, constitutive laws, etc. [26–30]. The phenomenon complexity implies, necessarily, a splitting of the modelling into two or more different spatial scales: macro-scales of many meters wide or more and smaller scales of few centimetres wide or less. Very accurate local calculation, at a small scale, based necessarily on CFD, along with the stochastic determination of mechanical parameters [31–35], could be used to construct "experimental–numerical laws" to be introduced in simplified models like Shallow Water [26–40]. Turbulence is an important phenomenon that is not completely understood through physical, mathematical, and numerical points of view. With the numerical viewpoint, the most accurate approach is the Direct Numerical Simulation (DNS) of fluid and particle flows [40–43]. On the other hand, its application on large or medium scales is not very practical due to a very high CPU time and memory required for either a high or medium Reynolds number. Some effective alternatives have been proposed. Among these, the Reynolds-Averaged Navier—Stokes (RANS) approach has

been proposed to simplify the related numerical simulations, including, in some way, the turbulence phenomenon. In [44], among many others, using the RANS approach, some useful insights have been gained, particularly about the impact of sediment distribution on the cross-sectional profile of a flow, both under laminar and turbulent conditions. The main algorithms were based on the numerical solutions of 5 equations: one related to mass conservation; two related to momentum balance along the horizontal (x) and vertical (y) coordinates; one related to the production, diffusion, and transport of turbulent kinetic energy; and the last one related to the dissipation of the turbulent energy. However, even this simplified 2D balanced equation approach is very demanding from the points of view of both the processing and necessary computation times required to run simulations at spatial and temporal scales that could involve wet debris flow phenomena, even fast. Thus, another mathematical–numerical approach is provided by the so-called "Reduced Complexity Models (RCMs)", through the "Cellular Automaton (CA)" approach [45–47]. The CA is suitable also for analysing landscape evolution through a grid of interacting cells, indicative of the mechanical and morphological characteristics of the selected location. Interactions between cells (automata) are governed by simplified versions of the related laws of physics. The equations used to represent the path of water and sediment are often simple. However, the implementation of these equations can introduce unexpected complexity into the model behaviour. CAs have also been used in the field of river dynamics [48].

Accordingly, several effective alternatives of intermediate difficulty among the approaches described above have been proposed. These include the Shallow-Water modelling, implemented in the software RAMMS, which was selected to carry out the simulations discussed in this paper. Accordingly, in the following sections, brief descriptions of the adopted mathematical modelling are reported.

3.2.1. Shallow-Water Model

The RAMMS solver is based on an efficient second-order numerical solution of the depth-averaged equations of motion for granular flows (Shallow-Water Approach). Flow heights and velocities are calculated on three-dimensional digital terrain models. The Release Areas of single or multiple blocks (debris flow initiation) can be easily specified using GIS-type tools. Alternatively, as in the case of the present paper, an assumed, suitable input hydrograph can be used to specify the flow rate as a function of time. The software also provides useful general information about the simulations, such as the released volume, flow behaviour (maximum flow velocities, dynamic pressure, and heights), and shutdown behaviour (mass flow). The selected rheological model is based on the two-parameter Voellmy relationship, including the erosion and friction processes of moving debris. To calibrate the Voellmy model of RAMMS, a geological site survey to ascertain the effects and extent of debris flow runout was carried out. The resulting 2D hydrodynamic equations, in the standard approach, are written in global coordinates as follows:

$$\frac{\partial U}{\partial t} + \frac{\partial F(U)}{\partial x} + \frac{\partial G(U)}{\partial y} = S_b + S_\tau \tag{1}$$

$$U = \left(h,\ hv_x,\ hv_y\right)^T \tag{2}$$

$$F = \left(hv_x,\ hv_x^2 + \frac{1}{2}g_\alpha h^2,\ hv_x v_y\right)^T;\ G = \left(hv_y,\ hv_x v_y,\ hv_y^2 + \frac{1}{2}g_\alpha h^2\right)^T \tag{3}$$

$$S_b = \left(0,\ \frac{p_{bx}}{\rho},\ \frac{p_{by}}{\rho}\right)^T;\ \frac{p_{bx}}{\rho} = -g_\alpha h\frac{\partial z_{bed}}{\partial x};\ \frac{p_{by}}{\rho} = -g_\alpha h\frac{\partial z_{bed}}{\partial y} \tag{4}$$

$$S_\tau = \left(0, -\frac{\tau_{bx}}{\rho}, -\frac{\tau_{by}}{\rho}\right)^T;\ \tau_{bx} = \rho g_\alpha h\frac{n^2 v_x\sqrt{v_x^2+v_y^2}}{h^{4/3}};\ \tau_{by} = \rho g_\alpha h\frac{n^2 v_y\sqrt{v_x^2+v_y^2}}{h^{4/3}} \tag{5}$$

Here, (1) is the matrix equilibrium equation. Equation (2) is the transpose of the U vector, whose components are the conserved variables representing the depth of flow in the z-coordinate; (v_x, v_y) are the velocity components along the x- and y-coordinates; the vector (hv_x, hv_y) is the resulting unit runoff; $g_\alpha = g \cdot cos^2(\alpha)$ is the projection of gravity acceleration along the normal bed forming an angle α with the vertical; this kind of gravity acceleration term is very important to preserve the accuracy of numerical predictions when the simulation involves steep slopes (more details can be found in [33]). Next, in (3), F and G are the flows along the x- and y-coordinates, respectively; $\frac{1}{2} g_\alpha h^2$ is a flow component obtained after assuming a hydrostatic pressure distribution in each water column, as a common practice in *Shallow-Water* models. Furthermore, (4) and (5) are the source terms $p_{b\,x}[Pa]$, $p_{b\,y}[Pa]$ incorporating the effects of pressure forces and bed slopes $\frac{\partial z_{bed}}{\partial x}$ of the lower level, while $\tau_{b\,x}[Pa]$ and $\tau_{b\,y}[Pa]$ are the tangential stresses characterised by the selected laws, one of the most common of which is the Manning's Coefficient, given in (5), where n is Manning's Coefficient, which usually takes into account the effects of bed roughness, internal friction, and changes in the shape and size of the channel cross-section. In some cases, the coefficient n was partially used as a calibration parameter to adapt the numerical results to the measured data.

3.2.2. Rheology

The most common models of mud-detrital fluids are considered as a hyper-concentrated mixture of water and sediment, possibly also affected by stop-and-go mechanisms and internal and bottom friction. From a numerical point of view, it is important to note that this topic belongs to the free-surface flow approach. Furthermore, the simulation of dry–wet transitions must be considered. Usually, in order to simplify the development of the necessary algorithms, the model makes the following assumptions: (a) the flow is confined to a thin layer with respect to the horizontal scale of interest; (b) the mixture of water and sediment is assumed to be a single homogeneous phase with constant properties, e.g., density, yield, stress, etc., and is described by a continuous approach, governed by Equation (1); (c) the velocities of the liquid and solid phases are assumed to be equal. To study the dynamic characteristics of wet debris flows, it is necessary to explore the models proposed within the framework of so-called Rheological Science. Therefore, due to the characteristics of the material of which the resulting debris flow is composed, the most suitable constitutive equations can be found among the models of incompressible non-Newtonian viscous fluids, for which a direct proportionality between deviatoric stress and flow velocity is not satisfied through the viscosity coefficient μ.

Accordingly, a wide rheological class of fluids can be described in terms of non-Newtonian viscosity, such as the models below (for example, [49–51]):

1. Full Bingham: For this option τ_{bx} and τ_{by} are the solutions of the following system, where τ_{yield} is the threshold value of the yield stress beyond which the material starts flowing. Once flowing, the movement is characterised by the Bingham viscosity μ_B of the mixture.

$$2\tau_{bx}^3 - 3\left(\tau_{yield} + 2\mu_B \frac{v_x}{h}\right)\tau_{bx}^2 + \tau_{yield}^3 = 0; \quad 2\tau_{by}^3 - 3\left(\tau_{yield} + 2\mu_B \frac{v_y}{h}\right)\tau_{by}^2 + \tau_{yield}^3 = 0 \tag{6}$$

2. Turbulent, where c_f is a friction coefficient:

$$\tau_b = \rho c_f \left(v_x^2 + v_y^2\right) \tag{7}$$

3. Coulomb turbulent, where θ is the bed slope angle and θ_b is the friction angle of the solid material:

$$\tau_b = \rho c_f \left(v_x^2 + v_y^2\right) + min(\tau_{yield}, g\rho h \cdot cos\theta \cdot tan\theta_b) \tag{8}$$

A much more detailed and accurate approach has been discussed in [52], which, however, cannot be included in large-scale spatial simulations Another commonly utilised expression, introduced into RAMMS and selected for all simulations carried out in this work, is the Voellmy fluid friction model discussed by Salm [52–54]. This model divides friction resistance into two parts: dry friction μ (dimensionless) of the Coulomb type and a resistance squared to the velocity or viscous–turbulent friction (ξ coefficient). Therefore, the friction resistance $\tau_b[Pa]$ takes on the following expression:

$$\tau_b[Pa] = \mu \cdot \rho hg \cdot cos\beta + \frac{\rho g \cdot \left(v_x^2 + v_y^2\right)}{\xi} \quad (9)$$

where ρ is the density; g is the gravitational acceleration; β is the slope angle; h is the flow height; v_x and v_y, is the flow velocities in the x- and y-directions; and $\rho hg \cdot cos\beta$ is the normal stress on the sliding surface. Voellmy's basic equation was modified by Bartelt [54–56] to include an effect related to cohesion through the additional term:

$$(1 - \mu) \cdot N_0 \cdot \left[1 - e^{-\left(\frac{\rho hg \cdot cos\beta}{N_0}\right)}\right] \quad (10)$$

where N_0, called yield stress, is a fitting parameter that defines the position of the shear curve inflection point. Therefore, N_0 acts as the yield strength, while μ acts as a hardening parameter. Furthermore, N_0, by increasing the shear stress, causes the flow to stop sooner. The Voellmy model considers the resistance of the solid phase (μ is also sometimes expressed as the tangent of the internal shear angle) and a viscous phase or turbulent fluid phase (ξ was introduced by Voellmy using hydrodynamic arguments). The friction coefficients are responsible for the behaviour of the flow. μ prevails when the flow is close to stopping, and ξ prevails when the flow is flowing rapidly. The Table 1 shows some reference values.

Table 1. Viscous–turbulent friction parameters ξ and μ.

	Granular Flow (Solid-Like)	**Earth Flow (Fluid-Like)**
Viscous–turbulent friction ξ [m/s^2]	100–200	200–1000
Dry friction of Coulombian type μ [non-dimensional]	0.05–0.4	

Throughout the simulation, the friction parameter of a calculation domain is constant within the time. However, it is possible to add up to two polygons within the calculation's geometrical domain with different friction parameters. For this work, this kind of option was selected. Voellmy's friction model has found wide application in the simulation of mass movements. Accordingly, the new equation, replacing the expression S_τ in (1) and (5), thus introducing an average value of the components along x and y, is as follows:

$$\tau_{bi}[Pa] = \mu \cdot \rho hg \cdot cos\beta i + \frac{\rho g \cdot \left(v_x^2 + v_y^2\right)}{\xi} + (1 - \mu) \cdot N_0 \cdot \left[1 - e^{-\left(\frac{\rho hg \cdot cos\beta i}{N_0}\right)}\right]; \; i = 1, \; 2 \quad (11)$$

where β_1 and β_2 are the slope angles along x and y, respectively. However, several other models have been proposed and applied in the literature to simulate the non-linear visco-plastic behaviour of fluids in terms of non-Newtonian viscosity. In [55,56], to simulate the behaviour of a mudflow, assumed to be incompressible, the constitutive Herschel–Bulkley law, modified by Papanastasiou [57] to regularise the viscosity (which would otherwise diverge to infinity for strain rates close to zero), was selected very effectively:

$$\begin{aligned} \eta\ [Pa \cdot s] &= \left\{ K\left[\sqrt{2Tr\left(\dot{\varepsilon}^2\right)}\right]^{(n-1)} + \frac{\tau_c}{\sqrt{2Tr\left(\dot{\varepsilon}^2\right)}} \right\} \cdot \left\{ 1 - exp\left[-B \cdot \sqrt{2Tr\left(\dot{\varepsilon}^2\right)} \right] \right\} \\ \tau\ [Pa] &= 2 \cdot \eta \cdot \dot{\varepsilon} \quad if \quad \sqrt{2Tr(\sigma^2)/2} > \tau_c \\ \dot{\varepsilon}\ [s^{-1}] &= 0 \quad if \quad \sqrt{2Tr(\sigma^2)/2} \leq \tau_c \end{aligned} \tag{12}$$

where η is the local regularised dynamic viscosity of the fluid; τ_c is the yield stress; K is the consistency of the fluid; n is the power law index; $\dot{\varepsilon} = \partial/\partial t\varepsilon$ is the strain rate tensor, in Cartesian coordinates, which is calculated by deriving each term of the tensor ε with respect to time; and parameter B (equal to 10 in [56]) relates to the maximum viscosity returned by regularisation when the strain rate is zero.

3.2.3. Erosion

The erosion module of RAMMS predicts the depth of sediment erosion caused by debris flows. Since RAMMS is used for hazard mapping in Switzerland, it must be used according to existing calculation guidelines in Switzerland. For this reason, the Voellmy–Salm (VS) model was implemented in RAMMS, which is used in the Swiss guidelines for calculating avalanche runout. However, it should be noted that in practical applications, the VS model has proven to be simple (it contains only two flow parameters) and numerically accurate. Field observations indicate that the erosion depth increases with the flow strength, e.g., with basal shear stress [58–60], and that the erosion rate can be very rapid [61]. Other observations indicate that small debris flows do not always erode sediments [62], so the model includes a critical shear stress that allows erosion only when the shear stress in a specific cell exceeds the critical shear stress value for triggering. The erosion algorithm predicts the maximum potential depth of erosion as a function of the calculated basal shear stress in each grid cell:

$$\begin{cases} e_m = 0 & \text{for } \tau < \tau_c \\ e_m = \frac{dz}{d\tau}(\tau - \tau_c) & for\ \tau \geq \tau_c \end{cases} \tag{13}$$

The potential erosion depth $dz/d\tau$ (per kPa) controls the vertical erosion rate (in the z-direction) as a linear function of the channel bed shear stress. Sediment is dragged until the erosion depth e_m is reached:

$$\frac{dz}{d\tau} = 0.025 \text{ for } e_t \leq e_m \tag{14}$$

where e_t is the depth of erosion (relative to the start of the simulation) at time t, and z is the vertical coordinate. If the shear stress in each cell is exceeded after erosion, the maximum erosion depth (relative to the initial bed elevation at the start of the simulation) is automatically adjusted, and further erosion can take place until the new value of e_m. In the selected version of RAMMS, the channel bed elevation does not change during the simulation. Therefore, for the simulations performed and discussed in this paper, topographic variation was not considered. However, users can incorporate changes in topography due to erosion or deposition, e.g., for further use in hazard modelling or event analysis scenarios, by selecting the post-processing options "Results → Add deposition to DEM" or "Results → Subtract erosion from DEM" or both with "Results → Add topographic changes (erosion/deposition) to DEM". Moreover, it is worth noting that it might be useful to apply a probabilistic approach, using the Weibull distribution as proposed in [63–65], to estimate the grain size of the eroded particles, which, in turn, has an impact on the velocity profile of a wet debris flow.

3.3. Channel Curvature

The total normal force N includes the centrifugal forces resulting from the curvature of the terrain. The method proposed in [14] was developed specifically for RAMMS. The module of the centrifugal acceleration, vector $\mathbf{a_c}$, is a function of both the flow velocity and terrain curvature. The centrifugal acceleration is calculated according to the following law:

$$|a_c| = u^T \cdot K \cdot u \tag{15}$$

where u is the velocity vector, u^T the transpose, and the K matrix describes the curvature of the track in all directions, including the "torsion" of the channel. The module of the resulting centrifugal force is then:

$$|F_c| = \rho\, h\, |a_c| \tag{16}$$

where ρ is the density of the wet debris flow, while h is the height of the flow. The force $F_\mathbf{c}$ is added to the normal force N. Typically, this increases friction, causing the debris flow to slow down in tortuous and twisted flow paths. It can change the position of the deposition once the flow leaves the gully. The curvature can be activated/deactivated in the window Run Simulation or via the "Help Advanced Curvature" menu.

3.4. Numerical Models

The numerical solutions of the common mathematical models require, usually, the discretisation of the continuum by grids. The physical quantities of interest (tension, displacements, etc.) are calculated in the resulting nodes. The domain is covered through elementary geometric elements ("mesh"), such as triangles, polygons, or simple 3D prisms. The most common approaches are the FEM, the Finite Difference Method (FDM), the Finite Volume Method (FVM), the Boundary Element method (BEM), and the Spectral Element Method (SEM), applied in seismic analyses. An excellent numerical reference, in which the cited methods are described, is provided in the book [66]. As an alternative, methods have been proposed that avoid the cumbersome construction of structured [67] or Delaunay-type meshing [68], called "mesh-free" methods, to solve the same differential equations. These include Smoothed Particle Hydrodynamics (SPH), among many others [56,67,69–73], and the Particle Finite Element Method (PFEM) [74,75].

In short, the solution of differential equations by means of the FEM, including those simulating the behaviour of a debris flow, requires the discretisation of the domain of interest, either in the Eulerian approach or in the Lagrangian approach, by means of geometric elements (tessellation) [76,77]. In order to obtain numerically correct results, it is necessary that the geometric elements used, such as triangles, rectangles, or polygons, are characterised by regularity as far as possible, e.g., they should be like equilateral triangles, squares, regular hexagons, etc. [78,79]. However, during a transient, the geometric elements may undergo deformations that make the discretisation no longer numerically adequate. Therefore, meshless methods have been proposed, among them SPH, which discretise the domain of interest by means of nodes (particles) to which all information is associated. The drawbacks of SPH, not present in FEM, are the boundary conditions, as discussed in [56,80]. The PFEM approach, based on nodes (particles) connected to each other by means of the FEM, with an update of the discretisation when the geometric elements are excessively deformed, includes all the advantages of both "meshing" and "mesh-free" methods. For the sake of completeness, within the subsequent sections, a brief description of both the SPH method and the FEM are reported. The SPH approach and, similarly, the PFEM are particularly suitable for simulated flows like wet debris flows, while FEM is the implemented method in RAMMS on which the numerical solution of the differential equations is based.

3.4.1. Brief Description of SPH

SPH is a meshless method that employs particles, the nodes of the discretisation, to transport information in the fluid flow domain. It has a Lagrangian nature, and this offers some important advantages: particles are moved at each time step according to their velocity, creating a grid that moves with the flow. The material derivatives are integrated directly in time. This avoids the need to evaluate non-linear convective terms. All these features make the SPH particularly interesting for simulating flows with high surfaces and deformation rates like wet debris flow. A field function is interpolated by means of a convolution integral with a kernel function. The integral is discretised over the particles:

$$f(\underline{x}) \cong \int_{\Omega x} f(\underline{x}') \cdot W(\underline{x} - \underline{x}') d\underline{x}' \cong \sum_{j=1}^{n} f\left(\underline{x}_j\right) \cdot W\left(\underline{x}_i - \underline{x}_j\right) dV_j \tag{17}$$

where $f(\underline{x})$ is the field function, such as density or velocity; $\underline{x}$ is the vector of coordinates in which the function $f(\underline{x})$ is calculated; $\underline{x}'$ is the vector of coordinates of all points (particles) within a bell-shaped function $W(\underline{x} - \underline{x}')$, called the Kernel, which vanishes outside the compact medium; '*i*' is the index of the particle that is at the point whose coordinates are included in the vector $\underline{x}$, while '*j*' it is the index of the particles that are at the points $\underline{x}'$; 'n' is the number of particles '*j*' contained in the bell-shaped function, which exchange information (e.g., momentum) with the particle i^{th}, whose influence is weighted according to distance $(\underline{x} - \underline{x}')$; $\Omega_{\underline{x}}$ is the global volume, while V_j is the "discrete" volume intercepted by $W(\underline{x} - \underline{x}')$. In reality, $W(\underline{x} - \underline{x}')$ is the numerical expression of the δ Dirac function. The smoothing length that defines the width of the bell and, thus, the number of particles '*n*' that are assumed to influence the behaviour of the *i*-th particle is a kernel parameter that also defines the scale of the interpolation length. The best resulting equations are as follows:

$$\frac{D\rho_i}{Dt} = -\sum_{j=1}^{n} m_j \cdot \left(\underline{\mathbf{v}}_j - \underline{\mathbf{v}}_i\right) \cdot \nabla_i W_{ij} + \sum_{j=1}^{n} m_j \cdot \underline{n}_{ij} \cdot \nabla_i W_{ij} \left(\frac{c_{ij}}{\rho_j}(\rho_j - \rho_i)\right) \tag{18}$$

$$\frac{D\underline{\mathbf{v}}_i}{Dt} = \underline{\mathbf{f}}_i - \sum_{j=1}^{n} m_j \cdot \left(\frac{p_i}{\rho_j^2} + \frac{p_j}{\rho_j^2}\right) \cdot \nabla_i W_{ij} + \sum_{j=1}^{n} \frac{2\eta_i \eta_j}{(\eta_i + \eta_j)} \frac{\left(\underline{\mathbf{r}}_{ij} \cdot \nabla_{\underline{\mathbf{r}}_{ij}} W_{ij}\right)}{\left|\underline{\mathbf{r}}_{ij}\right|^2 \rho_i \rho_j} m_j \underline{\mathbf{v}}_{ij} \tag{19}$$

where $\frac{D\underline{v}_i}{Dt}$ is the derived material velocity with respect to time, and then it is the acceleration of the particle; m_j is the mass of the particle; and $\underline{r}_{ij} = \left(\underline{x}_i - \underline{x}_j\right)$ and $\underline{v}_{ij} = \left(\underline{v}_i - \underline{v}_j\right)$ are, respectively, the distance and relative velocity between the particle and the particles (Morris momentum conservation [80]). The terms of the summation can be interpreted as forces that the particle i^{th} exchanges with the particles j^{th}. The Lagrangian nature of the method allows free-surface flows to be reproduced very easily. Another advantage of the SPH method is that it can be easily adapted to reproduce different rheological behaviours of non-Newtonian flows, provided the correct viscosity values are used in the equations. However, an important disadvantage of the method is the imposition of boundary conditions [80]. This problem is circumvented by using the PFEM, as pointed out before. As is clear from Figure 7, reporting a comparison between SPH numerical simulations and an actual laboratory experiment of a Water Dam Break (freely adapted from [56,81], the SPH approach is very versatile for simulating material fragmentation even after very rapid processes and is, therefore, particularly suitable for simulating fast debris flows with sediment transport.

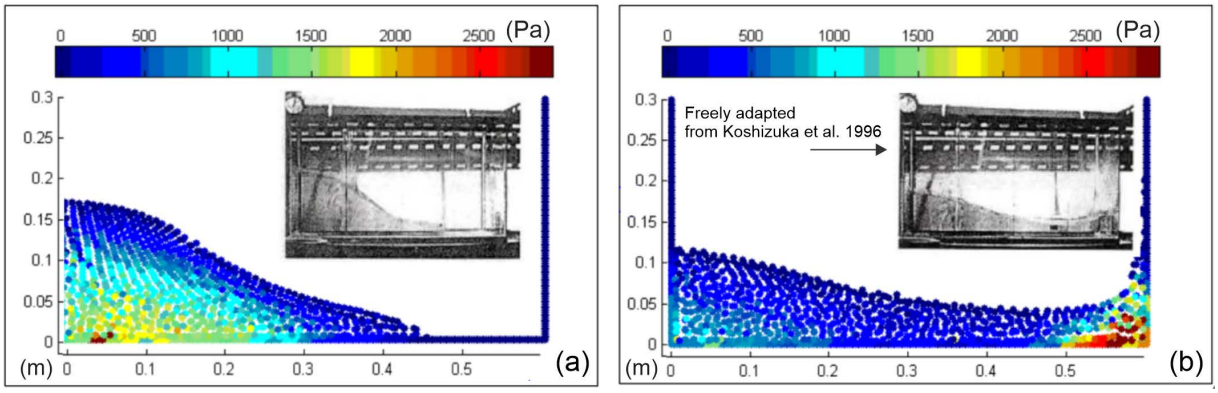


Figure 7. Comparison of the SPH numerical solution, freely adapted from [56], and experimental results for a fast dam break, freely adapted from [81], in the time range from 0.1 s to 1 s, respectively, from (**a**) to (**b**).

3.4.2. Brief Description of FEM

RAMMS software is based on the FEM approach. A commonly used variant of this method, aimed at solving the geometric part of the differential equations, is the Galerkin method (weak formulation), which is valid with some adjustments for the study of both solid- and fluid-type materials. The first step is the selection of the type of tessellation that covers the continuous spatial domain with elementary geometric elements, such as triangles, rectangles, and polygons in the 2D space and polyhedral, tetrahedra, and hexahedra in the 3D space (mesh). This is followed by the selection of the most suitable function, which is assumed to be the approximate solution of the differential equation to be solved in the selected elementary geometric element. Usually, the function identified is a polynomial, the degree of which is determined by the number of nodes located at specific points such as vertices, the medians of sides, but also at internal points. The degree of accuracy of the numerical solution, but also the demand for considerable computing power and memory, increases as the selected number of elements and nodes increases. These assumed approximations result in an "error" (called residual) of the solution of the differential problem with boundary condition constraints. Therefore, the resulting residual is weighted according to a function called the trial function (in the Galerkin method, it is based on the same selected interpolating function). Then, the integral of their product, performed over the entire geometric domain, is set to equal zero. It is shown that with this procedure, the residual due to the assumption of the form of the solution is minimised. Moreover, given the characteristics of the test functions, which are different from zero only in the element under consideration, the global integral is solved piecewise. The result is the transformation of the selected differential equation into a matrix equation, i.e., a system of algebraic equations whose unknowns are the numerical values that the variables of the problem taken on the nodes. The *i-th* algebraic equation contains the unknown associated with the *i-th* node and the unknowns associated with the nodes connected to it through the performed discretisation. Therefore, the problem that arises is the solution of the resulting matrix equations, also pursued iteratively, since the equations are usually not linear. The size of the matrix depends, obviously, on the number of nodes with which the discretisation was performed.

Finally, for the sake of completeness, it is worth adding that effective applications of Artificial Intelligence for optimising the parameters of constitutive equations have emerged in recent times [82,83] in different types of contexts.

4. RAMMS Simulations

4.1. RAMMS Simulation Settings and Parameters

As required input, the topographic surface was defined using the DEM with a 5 × 5 m resolution and loaded into the software. Simulations with RAMMS were conducted by

means of parametric analysis. This type of approach makes up for the lack of complete or partially complete information about the system and phenomenon studied. For this purpose, the simulations were divided into two macroscopic groups, assuming two different density values for the debris flow material: for the first group, a value of $\rho = 1200\ [\mathrm{kg/m^3}]$, and for the second group, $\rho = 1300[\mathrm{kg/m^3}]$, resulting in a different initial volume at the source area. To estimate the values of the main parameters, essentially rheological, as discussed in the previous paragraphs, criteria were selected to be associated with the final effects observed in situ of the flow under study, such as the final flow path and the partial filling of the mouth between the Rio Sonno and the Liri River. For both groups, the hydrograph mode was selected as the source input of material forming the debris flow.

The Figure 8 shows the 2D map of the discretisation of the domain under study. The term "detachment area" (area in red) was used to indicate the area from which the detachment of both 100 m^3 and 200 m^3 of material in approximately 44 s was assumed for the purpose of conducting sensitivity analyses. The area enclosed by the green dashed line follows the profile of the Rio Sonno, along which the debris flow was channelled. This area was automatically discretised by means of 1,143,905 triangular elements, with 1,146,048 associated nodes. For the description of the topography, the curvature option was activated, which allows the centrifugal force in the loops of the debris flow channel, expressed by Equation (12), to be considered.

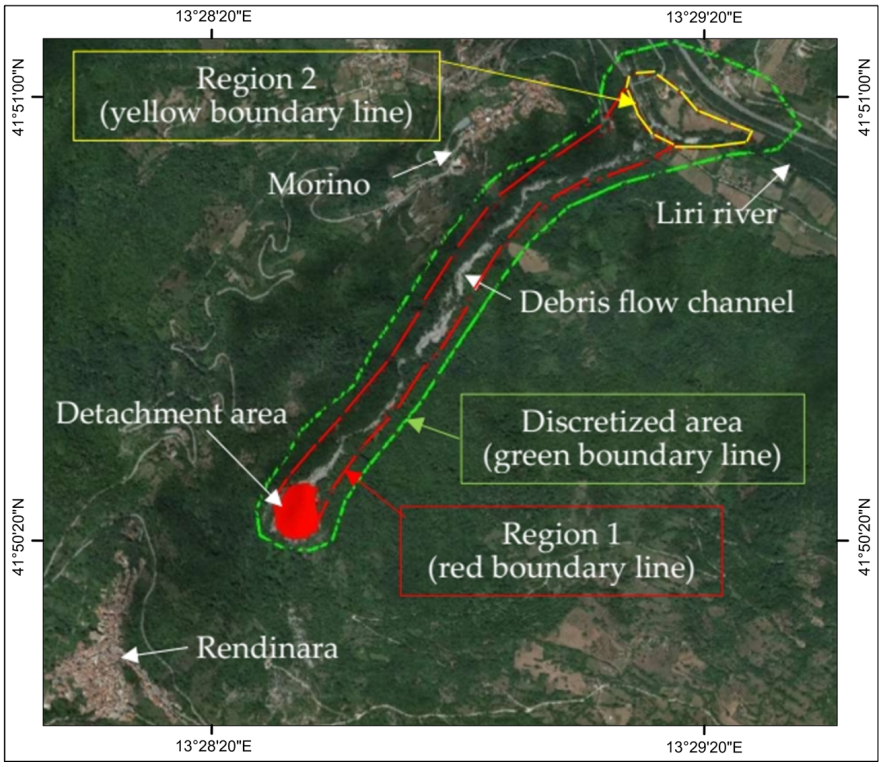


Figure 8. Discretisation map of the domain under study: detached (red) area; the discretised area included by the green lines, divided into two regions with different coefficients of friction; Region 1, area included by the dashed red lines; Region 2, area included by the dashed yellow lines.

In the discretised region, the FEM approach was applied for the solution of the Shallow-Water Equations. In order to also take into account the variation in the rheological characteristics of the flow, as far as possible with the selected code, the discretised region was divided into two regions: Region 1, characterised by $\mu = 0.01$ (dry friction of Coulombian type), which is included in the red dashed area, and Region 2, characterised by $\mu = 0.1$, which is included in the yellow dashed area (Figure 8). For both regions, $\xi = 200\ [\mathrm{m/s^2}]$ (viscous–turbulent friction) was selected. In the area outside the two re-

gions but included in the discretised area (green dashed line), default values were selected: $\mu = 0.2$ and $\xi = 500\ [\mathrm{m/s^2}]$. For all areas, the cohesion value $N_0 = 1000\ [\mathrm{Pa}]$ was selected (Equation (7)). In addition, the default values (bold marked) in Table 2 were considered for the erosion parameters. In general, the values attributed to the parameters are the results of various backfitting analyses, which are not reported, constrained by the requirement that the numerically calculated debris flow should terminate in the Liri River, not beyond the bridge shown in Figure 6c, as was evident from the geophysical investigations carried out on site. To carry out the simulations, after several attempts, the total duration of the transient and, consequently, the time-stopping criteria of the calculation, were chosen to be equal to the moment when the speed of the debris, at the mouth between the Rio Sonno and the Liri River, becomes negligible.

Table 2. Indications for the most appropriate choice of parameters simulating erosion in RAMMS (freely adapted from [10]).

Parameter	Description
Erosion density ($\mathrm{kg/m^3}$)	The default debris flow density is recommended unless more detailed information is available.
Erosion velocity: (m/s, default 0.025) - Loose and wet sediment (0.05 m/s) - Normal (0.025 m/s) - Dense sediment (0.013 m/s)	The speed at which debris flows drag material from the sedimentary bed: Very few values are available in the field, so a constant value based on experimental work (0.025 m/s) obtained for the Illgraben stream in Switzerland (erosion rates measured with sensors buried in the channel bed) is recommended. This is the rate that the model will use for dragging until the predicted erosion depth is reached. As this value increases, sediment will be dragged at a faster rate, potentially resulting in relatively large debris flows.
Potential erosion depth: (per kPa, default value 0.1) - Deep (0.2 per kPa) - Medium (0.1 per kPa) - Shallow (0.05 per kPa)	It controls the maximum potential erosion depth as a function of the maximum shear stress achieved in each cell: This value is the slope of the line that relates e_m to the maximum shear stress calculated for each cell. Changing the value of this parameter, for example, to 0.2 doubles the maximum potential erosion depth.
Critical shear stress: (kPa, default value 1.0) - Low (0.5 kPa) - Medium (1.0 kPa) - High (1.5 kPa)	Critical value at which erosion can begin: It is reasonable to expect that a channel bed of embedded boulders will have a higher critical shear stress, while a channel bed of saturated sandy gravel will have a lower value.
Maximum erosion depth: (m, default 0)	The maximum thickness of the erodible sediment layer can be set, if such data are available (e.g., in some cases, it may be known that there is only a limited amount of sediment available). The default value is 0, which means that the erosion algorithm calculates the maximum erosion depth by itself.

Further details on the mathematical models introduced in RAMMS are discussed in [64].

4.2. Release Input (Hydrograph/Block)

In RAMMS-Debris flow, there are two options for defining the initial conditions (release information) of a simulation: the Release Area (or block release) and Inlet Hydrograph. The starting conditions of a simulation can be selected according to the type of debris flow to be modelled. In general, it is useful to distinguish between un-channelled and channelled debris flows. Here, we use the term un-channelled debris flow for free-slope debris flows, while channelled debris flows develop in regions where streams limit flow paths and debris material mainly follow the stream channel, as in the selected test case. For a

channelled debris flow, it is more appropriate to use an Inlet Hydrograph. However, this requires knowledge of the amount of material (flow) flowing at a particular point. For a RAMMS simulation with a hydrograph, one has two options. Either the runoff at different times at a particular point is known, e.g., it is estimated from measured flow heights and corresponding channel cross-sections, or the estimated total volume is used in combination with empirical relationships between the total volume and maximum runoff. It is worth noting that many debris flows, when monitoring data are simplified, have a relatively simple triangular wave shape. Assuming a well-estimated total volume (e.g., field data), it is possible to calculate the maximum debris flow rate and the corresponding time to end. In nature, runoff hydrographs are generally best described by four points. However, a three-point hydrograph determines slightly higher heights and flow velocities after the maximum runoff. As described in the previous sections, the case studied concerns the evolution of a wet debris flow channelled into the bed of the Rio Sonno. Therefore, for the input related to the initial release of the material, the hydrograph was selected as the most suitable approach. In our case, the procedure chosen was to obtain, through simulations based on the numerical variation of the most influential parameters, a maximum height of about 4 m of the mass accumulated at the mouth between the Rio Sonno and the Liri river, at the end of the flow runoff time, i.e., when the flow velocity becomes negligible. The reference height was estimated by means of geophysical surveys. Several attempts were made, which are not reported in this paper, which led to the assumption of an initial released mass volume of 100 m^3, during an estimated time (based on engineering judgement) of approximately 44 s, peaking after 10 s. In addition, for a parametric analysis concerning the inventory of material evolving in debris flow, 200 m^3 was considered with the same timing. Accordingly, the resulting hydrograph, in Figure 9, was selected, in which the assumed released debris volume is indicated by the area subtended by the graph of flow trends.

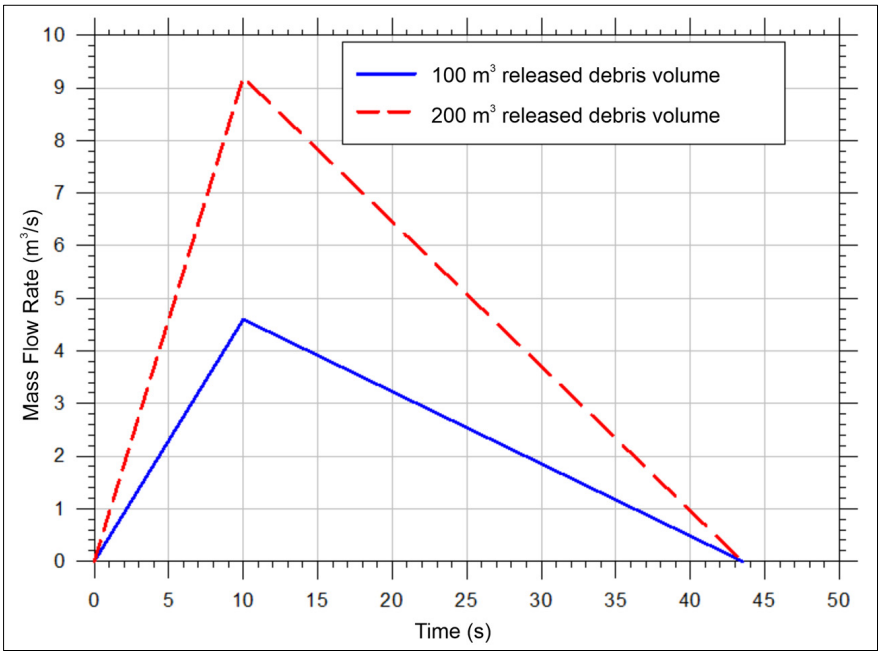


Figure 9. Assumed hydrograph, based on geophysical survey at the mouth between the Rio Sonno and Liri River.

5. Results

The features of the simulations carried out are shown in Table 3.

Table 3. Simulation parameter numerical values.

Simulation	Reference	Region 1/Region 2					
num.	Figure num.	Density kg/m^3	Vol. Source m^3	Max Time s	μ	ξ m/s^2	N_0 Pa
1	12 and 13	1200	100	800	0.01/0.1	200	1000
2	14	1300 vs. 1200	100	600	0.01/0.1	200	1000
	15	1300	100	1000	0.01/0.1	200	1000
	16	1300	100	300 vs. 1000	0.01/0.1	200	1000
	17	1200	200 vs. 100	800	0.01/0.1	200	1000
3	18	1200	200	800	0.01/0.1	200	1000
	19	1200	200 vs. 100	800	0.01/0.1	200	1000
	20	1200	200 vs. 100	800	0.01/0.1	200	1000

5.1. Debris Density $\rho = 1200\ Kg/m^3$

Figure 10 shows the coloured maps of the distribution of debris flow heights at different instances up to 800 s. It is observed that at 800 s, the debris has reached and invaded the area of the bridge over the Liri River, indicated in the figures by a white circle. In addition, between 600 and 700 s, in Figure 10d,e, material accumulation of approximately 4 m, indicated by a red colouring, already barring the Liri River, is observed. Figure 11 shows the maximum values of the velocities, pressures, and heights of the debris front, relative to an 800 s transient. As can be seen, the maximum debris flow velocity reached at the mouth between the Rio Sonno and the Liri River is negligible, as is the dynamic pressure (colouring of the legend), indicating the circumstance that the debris flow is progressively exhausted just around the mouth and the bridge, as verified by in situ investigations.

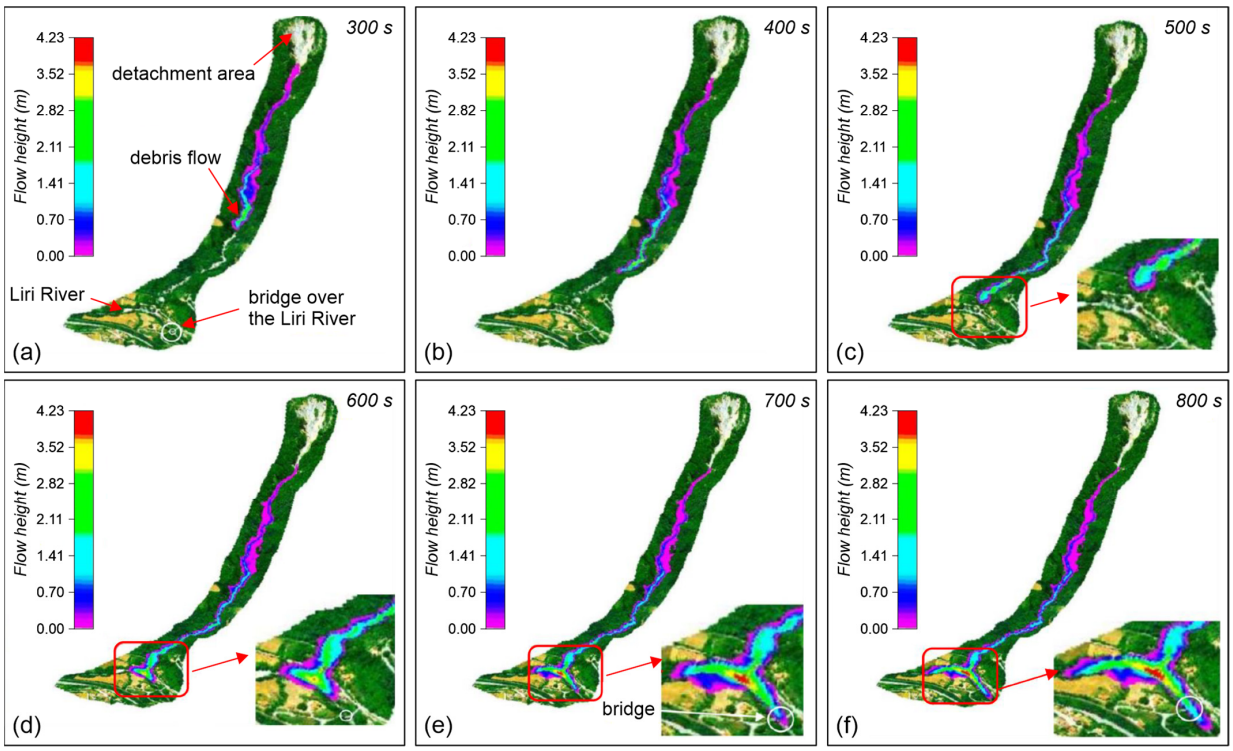


Figure 10. Flow height in the debris channel using a transitory time: 300 s (**a**), 400 s (**b**), 500 s (**c**), 600 s (**d**), 700 s (**e**) and 800 s (**f**).

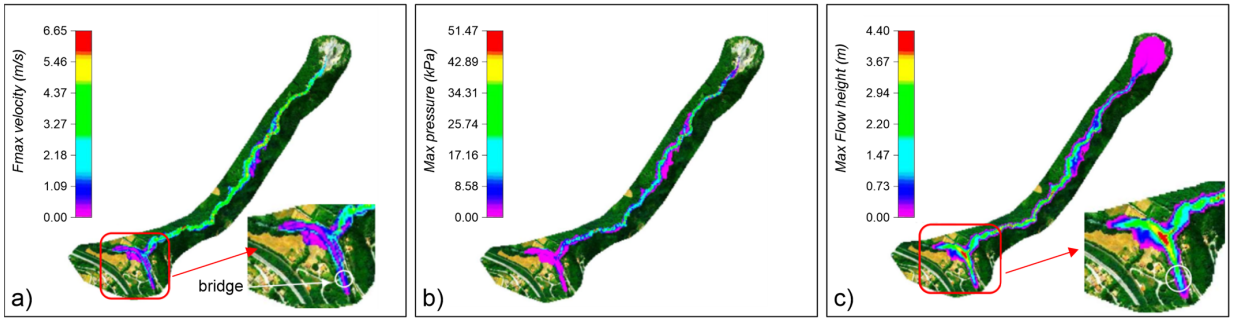


Figure 11. (**a**) Max. flow velocity; (**b**) max. flow pressure; (**c**) max. flow height, up to 800 s.

The legends of Figure 11 show the maximum values reached during the transient, i.e., 6.65 m/s and 51.47 kPa, for the velocity and dynamic pressure, respectively. These values are reached at certain points along the channel (Figure 11a,b). The maximum height of the front, about 4.4 m, is observed at the mouth.

5.2. Debris Density, $\rho = 1300\ Kg/m^3$

The Figure 12 shows a comparison of the results obtained after 600 s using two simulations that differ only in material density. The distribution is very similar, but the maximum height of the debris flow front with the assumption of a lower density is higher, 4.40 m versus 4.23 m. This occurrence may, evidently, depend on Coulomb friction, which is more intense the higher the weight is of the debris that covers the surface of the channel and, therefore, the higher the density of the debris. Accordingly, the friction force delays the arrival of the flow. Figure 13 shows the simulation at 1000 s. The debris flow, resulting from numerical simulation, would have reached areas of the bridge far beyond those actually reached. Consequently, with the numerical values selected, it would be possible to estimate the end of the runout, before 1000 s from the triggering of the flow. Figure 13 was reproduced from that which was directly shown in the Graphical User Interface (GUI) of RAMMS. All other figures were modified in their colouring and contrast to highlight details.

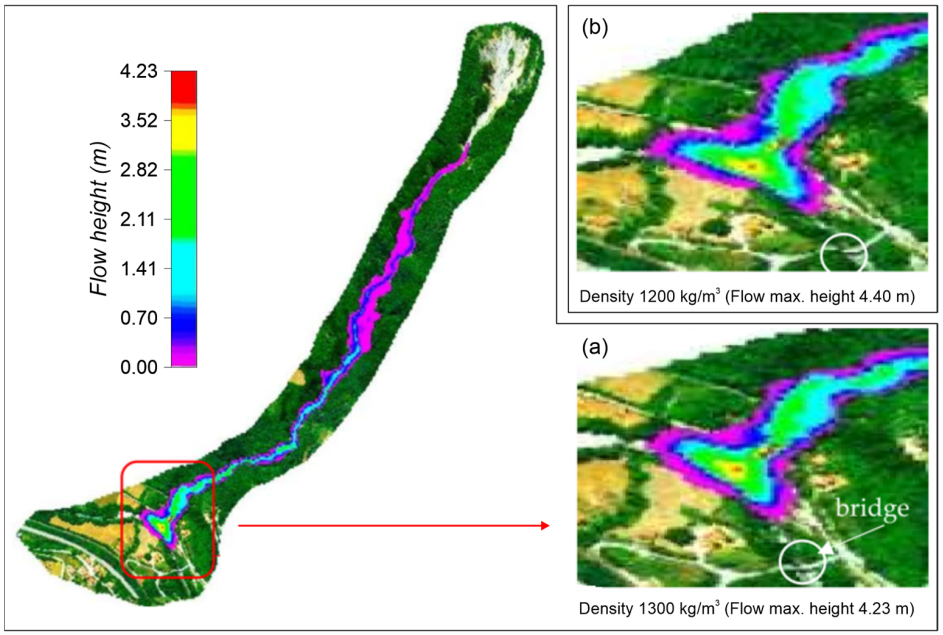


Figure 12. Flow height at 600 s. Comparison between different material density equal to 1300 kg/m^3 (**a**) and material density equal to 1200 kg/m^3 (**b**).

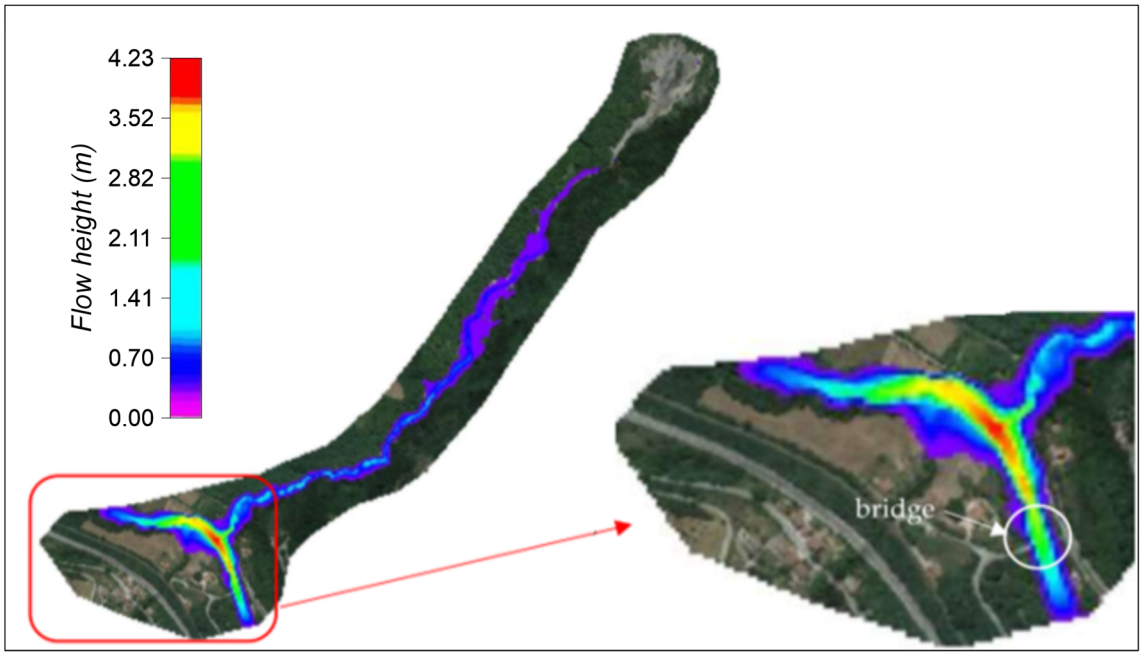


Figure 13. Flow height at 1000 s, density equal to 1300 kg/m^3, and total debris mass equal to 100 m^3.

As Figure 14a shows, after 300 s, the debris flow has not reached the mouth of the Liri River yet. At 1000 s, Figure 14b, the flow has stopped at the mouth between the Rio Sonno and the Liri River, but a very small part of the debris is still flowing, at a low speed, along the channel (about 1.5 m/s).

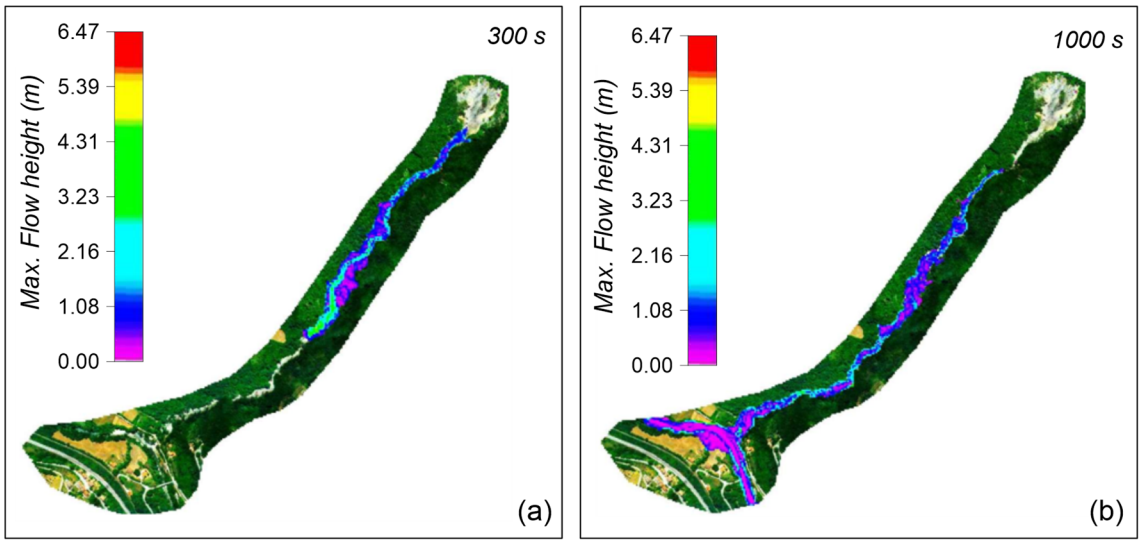


Figure 14. Comparison of the simulations between a velocity at 300 s (**a**) to a velocity at 1000 s (**b**).

A comparison of the results obtained assuming a total volume of debris released of 200 m^3 and a volume of 100 m^3 is shown in Figures 14 and 15. In particular, Figure 14 shows the height of the front after 800 s. No appreciable differences in the distribution of the material are apparent; however, the maximum peak of the material is slightly different, while Figure 16 shows the maximum values of the dynamic pressure and velocity. Figure 16b also zooms in on the area where the maximum velocity is reached.

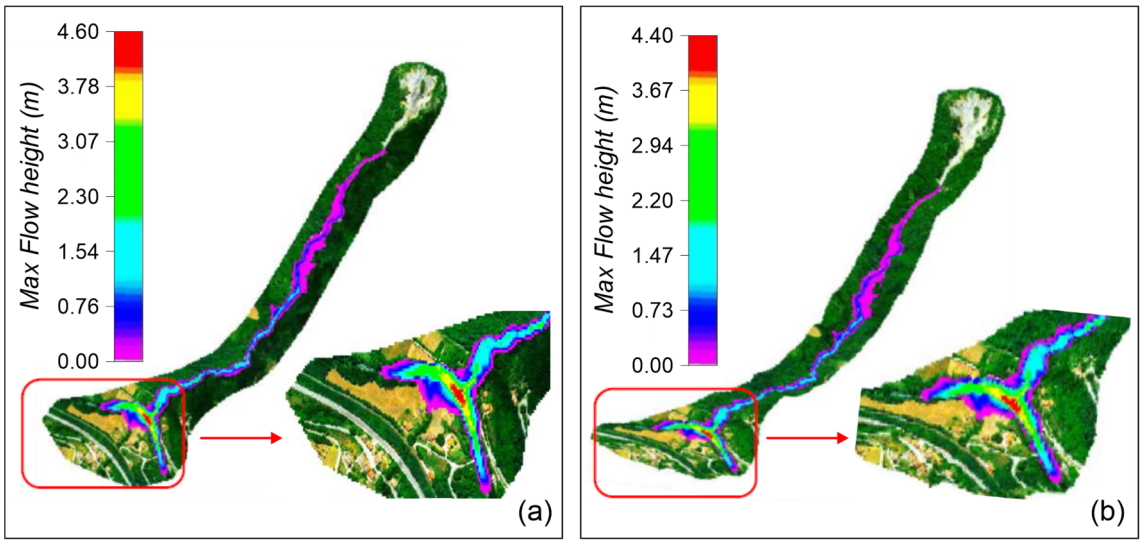


Figure 15. Flow height at 800 s, 1200 kg/m^3; comparison between 200 m^3 (**a**) and 100 m^3 (**b**) as initial released debris volumes.

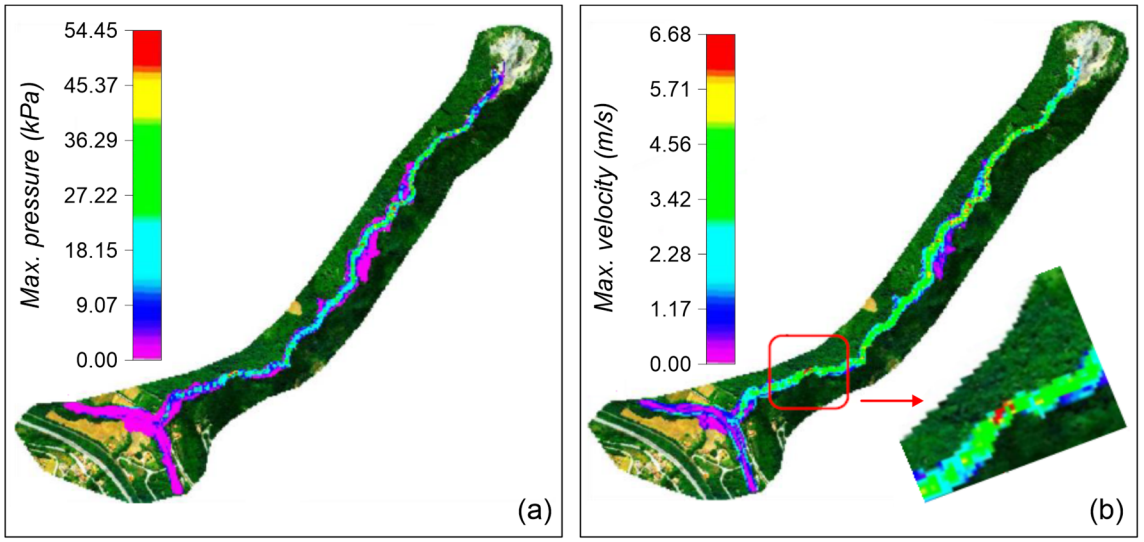


Figure 16. Max. pressures (**a**) and max. velocities (**b**) after 800 s, assuming a density of 1200 kg/m^3 and a volume of 200 m^3 of released debris.

Figure 17 shows the numerically predicted accumulations at the mouth of the Rio Sonno. The section considered is shown in yellow in Figure 17a and is indicated as the "debris flow cross-section". Since it is a straight segment, it does not necessarily intersect all points with the maximum heights of debris accumulation. However, the figures provide an acceptable indication of the obstruction caused by the flow. Furthermore, the results obtained assuming a density of 1200 m^3 and a total volume of 100 m^3 are compared with those obtained assuming a volume of 200 m^3 and the same density. The difference in the heights and widths of the accumulations, at least in the selected cross-section, are not proportional to the amount of material assumed to have been released. The material accumulates in a vertical direction, but also in a transverse direction, all along the way. Furthermore, the mathematical models are non-linear, thus invalidating any proportionality.

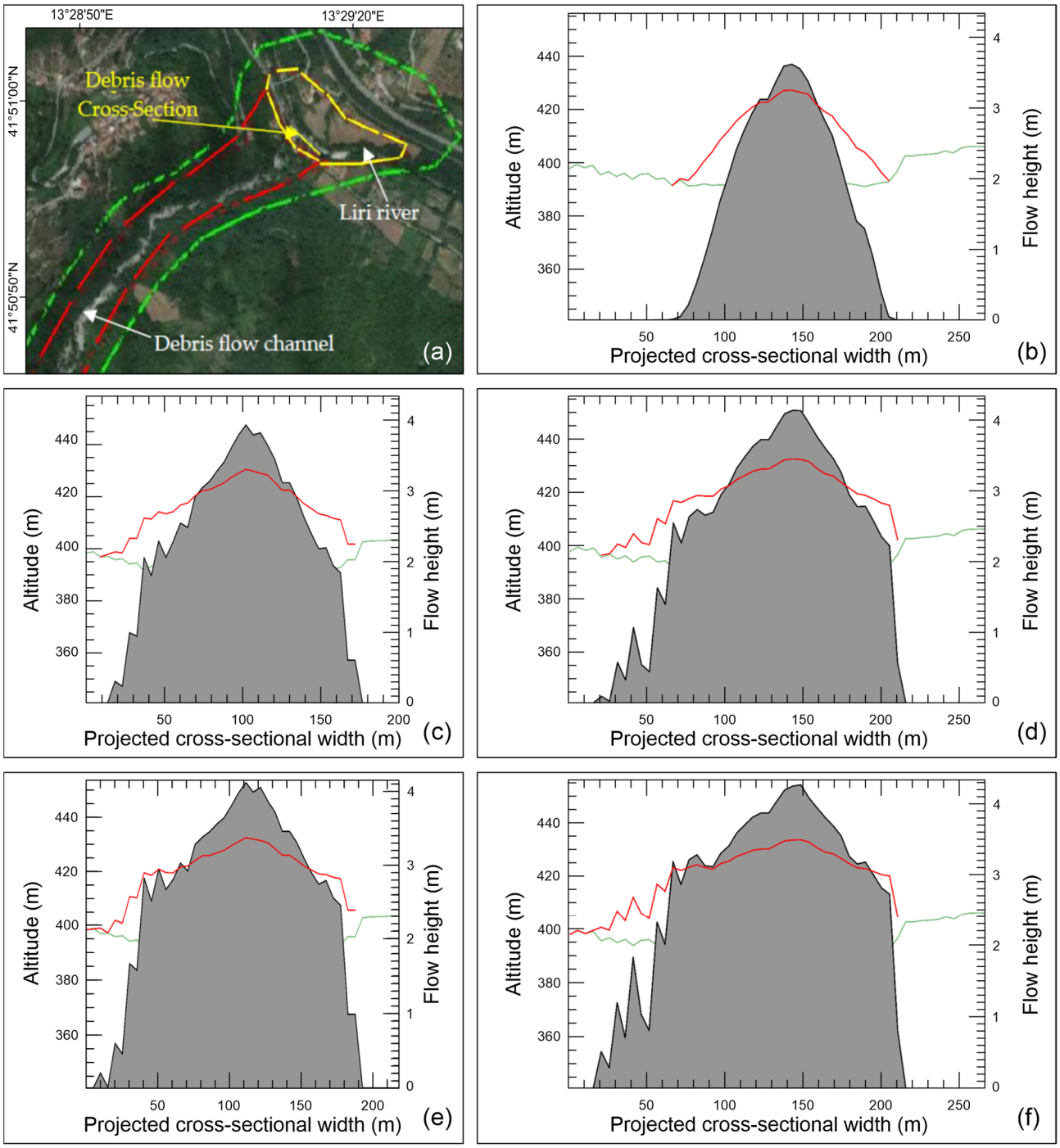


Figure 17. Accumulation along the debris flow cross-section, shown in yellow in Figure 17a. The grey fill is the cross-sectional flow height profile; the red line is the debris flow cross-sectional profile (multiple by 50) added to the debris channel topography; the green line is the cross-sectional debris channel topography. (**a**) Mouth of the debris flow. (**b**) Result for time 600 s and released mass 200 m^3. (**c**) Result for time 700 s and released mass 100 m^3. (**d**) Result for time 700 s and released mass 200 m^3. (**e**) Result for time 800 s and released mass 100 m^3. (**f**) Result for time 800 s and released mass 200 m^3.

Figure 18 shows the comparisons of the longitudinal profiles obtained numerically, at different instances, between the two different total volumes assumed for the parametric analyses. At 800 s, the maximum peak of the accumulation is less than 4 m, as shown in Figure 17f. The reason for this is, obviously, the choice of the longitudinal line and transverse segment. It is also worth noting that the legend with the coloured band indicates

shades with variations in the values of the heights, pressures, and velocities. However, it easy to observe that the results are consistent.

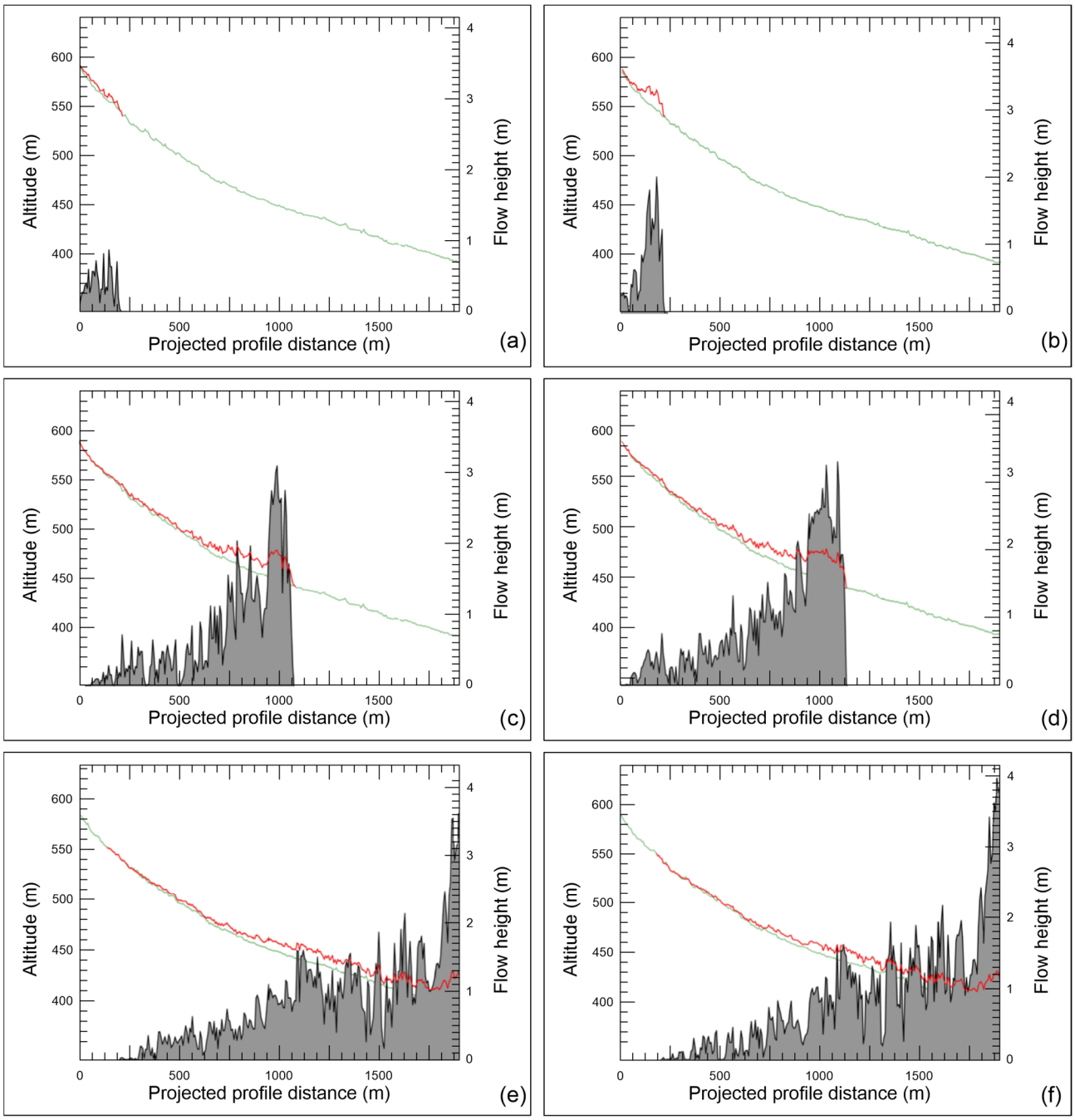


Figure 18. Longitudinal height profile, along a selected line drawn along the Rio Sonno path. The red line is the debris flow longitudinal profile (multiple by 50) added to the debris channel topography; the green line is the debris channel topography. (**a**) Result for time 100 s and released mass 100 m^3. (**b**) Result for time 100 s and released mass 200 m^3. (**c**) Result for time 300 s and released mass 100 m^3. (**d**) Result for time 300 s and released mass 200 m^3. (**e**) Result for time 800 s and released mass 100 m^3. (**f**) Result for time 800 s and released mass 200 m^3.

6. Discussion

For the selected test case, an accumulation of debris of approximately 4 m at the confluence between the Rio Sonno and the Liri River and the flooding of the bridge over the Liri River were estimated through in situ investigations and, accordingly, were assumed as

calibration targets. Three different types of parametric simulations were carried out using a back analysis approach to obtain the observed values and phenomena. The simulations were carried out by means of the RAMMS code, based on the mathematical model of "Shallow Water" with finite elements and the Voellmy–Bartelt rheological model.

As shown in the results section, starting from two different initial volume assumptions (100 and 200 m^3), both field observations and the results from [20] are confirmed. In both cases, the Liri River was obstructed by debris flow. In the study described in [17], the time range of the event would have been between 600 and 650 s, depending on the distance covered and rheological model assumed (Bingham). In this paper, however, due to a different choice of the rheological behaviour (Voellmy–Bartelt), the time range was estimated between 600 and 800 s. Furthermore, in both models, the debris accumulation caused the inundation of the bridge, as confirmed by local inspections.

According to the energy balance obtained from the simulations, the maximum dynamic pressure would have been 54 kPa, which indicates the maximum impact energy of the phenomenon on any obstacles along the channel. The maximum values were obtained numerically in the narrow zone of channel near, but before, the confluence with the Liri River. Furthermore, the resulting values of the maximum heights are approximately 3.3 m in [9] and 4.4 m in this work. Regarding the velocities, however, the differences are greater and range from a maximum value of 12 m/s in [17] to a maximum of 6.7 m/s in this work. These results can be explained in the context of the differences between the two selected techniques. However, in the evaluation model approach, which was selected to carry out these kinds of simulations focused on obtaining safer values, it can be argued that the results are both congruent.

7. Conclusions

The modelling approaches discussed in this article, including SPH approaches, are valid tools for assessing, in backfitting mode, the volumes of materials involved in the flow-feeding process, for the purpose of possible mitigation works (debris flow-type barrages, weirs, flow diversion, etc.).

Accordingly, these results provide a valuable foundation for assessing risks and developing effective mitigation measures that can reduce the effects of possible events of this kind. It can also aid in the localisation and parametrisation of early warning monitoring systems for potential debris flows. In fact, in the test case in question, the suggestion emerges to set up a pluviometric station (early warning) in the crest area, setting the warning thresholds based on the precipitation intensities recorded in the period 1–15 March 2021 (the period of the melt initiation) to check that the possible flow does not block the Liri River. Data limitations in this study are largely due to logistical challenges in accessing the upstream site of the debris flow. Despite these constraints, the uncertainty associated with this limited dataset was effectively mitigated by the field observations conducted downstream. Here, the filed measurements provided valuable insights, as the observed flow velocities and flow depth aligned closely with the model's simulation outputs, enhancing the model's credibility and reliability under the given conditions. Another limit is the assumption of a constant, unchanging topography throughout the event. Debris flows can cause significant changes in topography due to erosion or the deposition of material, which dynamically alters the shape of the channel and the flow conditions of the debris. The interaction can lead to results that could differ from those obtained under the assumption of constant topography.

In future analyses, it would be worth considering the inclusion of the variable topography in the simulations to allow for a more realistic representation of the phenomenon and more accurate predictions of its effects. Furthermore, our research could benefit by employing advanced technologies and more comprehensive analyses aimed at bridging the remaining data gaps. High-resolution remote sensing, real-time monitoring systems, and UAV-based surveys could provide enhanced spatial and temporal data coverage, supporting a deeper understanding of debris flow dynamics and improving predictive

capabilities for such events. In addition, comparisons will be made with other rheological models such as Bingham's. Finally, it is worth suggesting, for in-depth studies, the use of genetic-type algorithms for the optimisation of the sets of parameter values characterising the used mathematical models. The model under consideration is based on a set of physical parameters to which numerical values must be attributed to obtain simulations showing an accumulation of about 4 m at the mouth of the Rio Sonno with the Liri River and the partial reaching of the bridge by the debris. Genetic algorithms would be applied precisely in the choice of numerical values by means of the usual Artificial Intelligence techniques, while RAMMS or similar algorithms would have the function of Machine Learning, i.e., to learn and verify the consistency of the chosen values and indicate possible modifications.

Author Contributions: Conceptualisation, A.P. and N.S.; methodology, A.P. and M.M.; software, A.P. and M.M.; validation, N.S.; investigation, C.Z. and N.S.; resources, N.S.; data curation, M.M. and C.Z.; writing—original draft preparation, A.P.; review and editing, all the authors; funding acquisition, N.S. All authors have read and agreed to the published version of the manuscript.

Funding: This research received no external funding.

Data Availability Statement: Data will be made available on request.

Conflicts of Interest: The authors declare no conflicts of interest.

References

1. Guo, Z.; Ferrer, J.V.; Hürlimann, M.; Medina, V.; Puig-Polo, C.; Yin, K.; Huang, D. Shallow Landslide Susceptibility Assessment under Future Climate and Land Cover Changes: A Case Study from Southwest China. *Geosci. Front.* **2023**, *14*, 101542. [CrossRef]
2. Gariano, S.L.; Guzzetti, F. Landslides in a changing climate. *Earth-Sci. Rev.* **2016**, *162*, 227–252. [CrossRef]
3. Vuillez, C.; Tonini, M.; Sudmeier-Rieux, K.; Devkota, S.; Derron, M.H.; Jaboyedoff, M. Land use changes, landslides and roads in the Phewa Watershed, Western Nepal from 1979 to 2016. *Appl. Geogr.* **2018**, *94*, 30–40. [CrossRef]
4. Sciarra, N.; Mangifesta, M.; Carabba, L.; Mischiatti, L. Methodological Approach for the Study of Historical Centres of High Architectural Value Affected by Geo-Hydrological Hazards: The Case of Lanciano (Abruzzo Region—Central Italy). *Geosciences* **2022**, *12*, 193. [CrossRef]
5. Sha, S.; Dyson, A.P.; Kefayati, G.; Tolooiyan, A. Analysis of Debris Flow Protective Barriers Using the Coupled Eulerian Lagrangian Method. *Geosciences* **2024**, *14*, 198. [CrossRef]
6. Zito, C.; Mangifesta, M.; Francioni, M.; Guerriero, L.; Di Martire, D.; Calcaterra, D.; Pasculli, A.; Sciarra, N. Cascading Landslides at Morino-Rendinara, L'Aquila, Central Italy: Numerical Modelling of Slope-Scale Prospective Debris Flow Propagation. *Ital. J. Eng. Geol. Environ.* **2024**, *2024*, 285–293. [CrossRef]
7. Guo, Y.; Feng, Z.; Wang, L.; Tian, Y.; Chen, L. Hazard Assessment of Debris Flow: A Case Study of the Huiyazi Debris Flow. *Water* **2024**, *16*, 1349. [CrossRef]
8. Wang, J.; Zhen, J.; Hu, W.; Chen, S.; Lizaga, I.; Zeraatpisheh, M.; Yang, X. Remote sensing of soil degradation: Progress and perspective. *Int. Soil Water Conserv. Res.* **2023**, *11*, 429–454. [CrossRef]
9. Alam MJ, B.; Manzano, L.S.; Debnath, R.; Ahmed, A.A. Monitoring Slope Movement and Soil Hydrologic Behavior Using IoT and AI Technologies: A Systematic Review. *Hydrology* **2024**, *11*, 111. [CrossRef]
10. RAMMS (Rapid Mass Movement Simulation). Available online: https://ramms.slf.ch (accessed on 15 April 2024).
11. Cesca, M.; D'Agostino, V. Comparison between FLO-2D and RAMMS in debris-flow modelling: A case study in the Dolomites. *WIT Trans. Eng. Sci.* **2008**, *60*, 197–206. [CrossRef]
12. Franco-Ramos, O.; Ballesteros-Cánovas, J.A.; Figueroa-García, J.E.; Vázquez-Selem, L.; Stoffel, M.; Caballero, L. Modelling the 2012 lahar in a sector of Jamapa Gorge (Pico de Orizaba volcano, Mexico) using RAMMS and tree-ring evidence. *Water* **2020**, *12*, 333. [CrossRef]
13. Gan, J.; Zhang, Y.X. Numerical simulation of debris flow runout using RAMMs: A case study of Luzhuang gully in China. *Comput. Model. Eng. Sci.* **2019**, *121*, 981–1009. [CrossRef]
14. Fischer, J.-T.; Kowalski, J.; Pudasaini, S.P. Topographic curvature effects in applied avalanche modelling. *Cold Reg. Sci. Technol.* **2012**, *74*, 21–30. [CrossRef]
15. Gaume, J.; Gast, T.; Teran, J.; van Herwijnen, A.; Jiang, C. Unified modeling of the release and flow of snow avalanches using the material point method. In *Geophysical Research Abstracts*; Library for the Research Institutes within the ETH Domain: Dübendorf, Switzerland, 2018; Volume 20, pp. 1–5.
16. Sovilla, B.; McElwaine, J.N.; Schaer, M.; Vallet, J. Variation of deposition depth with slope angle in snow avalanches: Measurements from Vallée de la Sionne. *J. Geophys. Res. Earth Surf.* **2010**, *115*, 2010. [CrossRef]
17. Chen, H.; Crosta, G.B.; Lee, C.F. Erosion Effect on Runout of Fast Landslides, Debris Flows and Avalanches: A Nu-merical Investigation. *Géotechnique* **2006**, *56*, 305–322. [CrossRef]

18. Sharma, S.; Talchabhadel, R.; Nepal, S.; Ghimire, G.R.; Rakhal, B.; Panthi, J.; Kumar, S. Increasing risk of cascading hazards in the central Himalayas. *Nat. Hazards* **2023**, *119*, 1117–1126. [CrossRef]
19. Ulusay, R.; Sonmez, H. Modifications to the geological strength index (GSI) and their applicability to stability of slopes. *Int. J. Rock Mech. Min. Sci.* **1999**, *36*, 743–760.
20. Zito, C.; Mangifesta, M.; Francioni, M.; Guerriero, L.; Di Martire, D.; Calcaterra, D.; Sciarra, N. Cascading Landslide: Kinematic and Finite Element Method Analysis through Remote Sensing Techniques. *Remote Sens.* **2024**, *16*, 3423. [CrossRef]
21. Fabbi, S.; Galluzzo, F.; Pichezzi, R.M.; Santantonio, M. Carbonate intercalations in a terrigenous foredeep: Late Miocene examples from the Simbruini Mts. and the Salto Valley (Central Apennines—Italy). *Ital. J. Geosci.* **2013**, *133*, 85–100. [CrossRef]
22. Brandano, M.; Mateu-Vicens, G.; Gianfagna, A.; Corda, L.; Billi, A.; Quaresima, S.; Simonetti, A. Hardground development and drowning of a Miocene carbonate ramp (Latium-Abruzzi): From tectonic to paleoclimate. *J. Medi-Terranean Earth Sci.* **2009**, *1*, 47–56.
23. Carminati, E.; Corda, L.; Mariotti, G.; Brandano, M. Tectonic control on the architecture of a Miocene carbonate ramp in the Central Apennines (Italy): Insights from facies and backstripping analyses. *Sediment. Geol.* **2007**, *198*, 233–253. [CrossRef]
24. Centamore, E.; Rossi, D.; Tavarnelli, E. Geometry and kinematics of Triassic-to-Recent structures in the North-ern-Central Apennines: A review and an original working hypothesis. *Ital. J. Geosci.* **2009**, *128*, 419–432. [CrossRef]
25. Ikuemonisan, F.E.; Ozebo, V.C.; Olatinsu, O.B. Investigating and modelling ground settlement response to groundwater dynamic variation in parts of Lagos using space-based retrievals. *Solid Earth Sci.* **2021**, *6*, 95–110. [CrossRef]
26. Guo, J.; Wang, X.; Wang, J.; Dai, X.; Wu, L.; Li, C.; Li, F.; Liu, S.; Jessell, M.W. Three-dimensional geological modeling and spatial analysis from geotechnical borehole data using an implicit surface and marching tetrahedra algorithm. *Eng. Geol.* **2021**, *284*, 106047. [CrossRef]
27. Omar, P.; Gaur, S.; Dwivedi, S.B.; Dikshit, P.K.S. A Modular Three-Dimensional Scenario-Based Numerical Modelling of Groundwater Flow. *Water Resour. Manag.* **2020**, *34*, 1913–1932. [CrossRef]
28. Iliopoulos, I.; Mito, Y.; Hanratty, T. A stochastic model for solid particle dispersion in a nonhomogeneous turbulent field. *Int. J. Multiph. Flow* **2003**, *29*, 375–394. [CrossRef]
29. Thomson, D.J. Criteria for the selection of stochastic models of particle trajectories in turbulent flows. *J. Fluid Mech.* **1987**, *180*, 529–556. [CrossRef]
30. Du, S.; Sawford, B.L.; Wilson, J.D.; Wilson, D.J. Estimation of the Kolmogorovconstant (C0) for the Lagrangian structure function, using a second-order Lagrangian model of grid turbulence. *Phys. Fluids* **1995**, *7*, 3083–3090. [CrossRef]
31. Murillo, C.J.J.; Garcia-Navarro, P. 2D simulation of granular flow over irregular steep slopes using global and local coordinates. *J. Comput. Phys.* **2013**, *255*, 166–204.
32. Pasculli, A.; Cinosi, J.; Turconi, P.; Sciarra, N. Learning Case Study of a Shallow-Water Model to Assess an Early-Warning System for Fast Alpine Muddy-Debris-Flow. *Water* **2021**, *13*, 750–780. [CrossRef]
33. Pasculli, A.; Longo, R.; Sciarra, N.; Di Nucci, C. Surface Water Flow Balance of a River Basin Using a Shallow Water Approach and GPU Parallel Computing—Pescara River (Italy) as Test Case. *Water* **2022**, *14*, 234. [CrossRef]
34. Denlinger, R.; Iverson, R. Granular avalanches across irregular three dimensional terrain: 1. Theory and computation. *J. Geophys. Res.* **2004**, *109*, F01014. [CrossRef]
35. Mangeney-Castelnau Bouchut, F.; Vilotte, J.P.; Lajeunesse, E.; Aubertin, A.; Pirulli, M. On the use of Saint-Venant equations for simulating the spreading of a granular mass. *J. Geophys. Res.* **2005**, *110*, B09103.
36. Iverson, R.; Denlinger, R. Flow of variably fluidized granular masses across three-dimensional terrain. *A Coulomb mixture theory. J. Geophys. Res.* **2001**, *106*, 537–552. [CrossRef]
37. Schmeeckle, M.W.; Nelson, J.M. Direct numerical simulation of bedload transport using a local, dynamic boundary condition. *Sedimentology* **2003**, *50*, 279–301. [CrossRef]
38. Zohdi, T.I. Computational of strongly coupled multifield interaction in particle-fluid systems. *Comput. Methods Appl. Mech. Eng.* **2007**, *196*, 3927–3950. [CrossRef]
39. Moin, P.; Krishnan, M. Direct Numerical Simulation: A tool in Turbulence Research. *Annu. Rev. Fluid Mech.* **1998**, *30*, 539–578. [CrossRef]
40. Scardovelli, R.; Zaleski, S. Direct Numerical Simulation of free surface and interfacial flow. *Annu. Rev. Fluid Mech* **1999**, *31*, 567–603. [CrossRef]
41. Coleman, G.N.; Kim, J.; Spalart, P.R. Direct numerical simulation of a decelerated wallbounded turbulent shear flow. *J Fluid Mech.* **2003**, *495*, 1–18. [CrossRef]
42. Pasculli, A. CFD-FEM 2D Modelling of a local water flow. Some numerical results. *Alp. Mediterr. Quat.* **2008**, *21*, 215–228.
43. Pasculli, A. Viscosity Variability Impact on 2D Laminar and Turbulent Poiseuille Velocity Profiles; Characteristic-Based Split (CBS) Stabilization. In Proceedings of the 5th International Conference on Mathematics and Computers in Sciences and Industry (MCSI), Corfu, Greece, 25–27 August 2018. [CrossRef]
44. Wolfram, S. Statistical mechanics of cellular automata. *Rev. Mod. Phys.* **1983**, *55*, 601–644. [CrossRef]
45. Cook, M. Universality in Elementary Cellular Automata. *Complex Syst.* **2004**, *15*, 1–40. [CrossRef]
46. Crutchfield, J.P.; Hanson, J.E. Turbulent Pattern Bases for Cellular Automata. *Phys. D* **1993**, *69*, 279–301. [CrossRef]
47. Vichniac, G.Y. Simulating Physics with Cellular Automata. *Phys. D Nonlinear Phenom.* **1984**, *10*, 96–110. [CrossRef]

48. Audisio, C.; Pasculli, A.; Sciarra, N. Conceptual and numerical models applied on the river Pellice (Northwestern Italy). In *Engineering Geology for Society and Territory Volume 3: River Basins, Reservoir Sedimentation and Water Resources*; Springer: Berlin/Heidelberg, Germany, 2015; pp. 327–330. [CrossRef]
49. Hydronia, L.L.C. RiverFlow2D, Two-Dimensional Flood and River Dynamics Model, Reference Manual. Available online: www.hydronia.com (accessed on 3 October 2023).
50. Lacasta, A.; Morales-Hernández, M.; Juez, C.; Caviedes-Voullieme, D.; Fernández-Pato, J.; Murillo, J.; García-Navarro, P. Challenges and improvements on high-performance river flow numerical modelling. Road to a new era of computing using RiverFlow2D GPU. In Proceedings of the River Flow 2016, Iowa City, IC, USA, 22 June 2016.
51. Juez, C.; Ferrer-Boix, C.; Murillo, J.; Hassan, M.A.; García-Navarro, P. A model based on Hirano-Exner equations for two-dimensional transient flows over heterogeneous erodible beds. *Adv. Water Resour.* **2016**, *87*, 1–18. [CrossRef]
52. Salm, B. Flow, flow transition and runout distances of flowing avalanches. *Ann. Glaciol.* **1993**, *18*, 221–226. [CrossRef]
53. Voellmy, A. *Uber die Zerst Orungskraft von Lawinen*; Schweizer Bauzeitung: Zurich, Switzerland, 1955; pp. 73+159–165+212–217+246–249+280–285.
54. Bagnold, R.A. The shearing and dilatation of dry sand and the "singing" mechanism. *Proc. R. Soc. Lond. Ser. A* **1966**, *295*, 219–232.
55. Bartelt, P.; Vera Valero, C.; Feistl, T.; Christen, M.; Bühler, Y.; Buser, O. Modelling cohesion in snow avalanche flow. *J. Glaciol.* **2015**, *61*, 837–850. [CrossRef]
56. Minatti, L.; Pasculli, A. Dam break Smoothed Particle Hydrodynamic modelling based on Riemann solvers. Advances in Fluid Mechanics VIII, Algarve (Spain). *WIT Trans. Eng. Sci.* **2010**, *69*, 145–156. [CrossRef]
57. Papanastasiou, T.C. Flows of materials with yield. *J. Rheol.* **1987**, *31*, 385. [CrossRef]
58. Frank, F.; McArdell, B.W.; Oggier, N.; Baer, P.; Christen, M.; Vieli, A. Debris flow modelling at Meretschibach and Bondasca catchments, Switzerland: Sensitivity testing of field data-based entrainment model. *Nat. Hazards Earth Syst. Sci.* **2017**, *17*, 801–815. [CrossRef]
59. Prancevic, J.P.; Lamb, M.P. Unraveling bed slope from relative roughness in initial sediment motion. *J. Geophys. Res. Earth Surf.* **2015**, *120*, 474–489. [CrossRef]
60. Revellino, P.; Hungr, O.; Guadagno, F.M.; Evans, S.G. Velocity and runout simulation of destructive debris flows and debris avalanches in pyroclastic deposits, Campania region, Italy. *Environ. Geol.* **2004**, *45*, 295–311. [CrossRef]
61. Berger, C.; McArdell, B.W.; Schlunegger, F. Direct measurement of channel erosion by debris flows, Illgraben, Switzerland. *J. Geophys. Res.* **2011**, *116*, F01002. [CrossRef]
62. Berger, C. Debris Flow Entrainment and Sediment Transfer Processes at the Illgraben Ccatchment, Switzerland. Ph.D. Thesis, University of Bern, Institute of Geological Sciences, Bern, Switzerland, 2010.
63. Pasculli, A.; Sciarra, N. A probabilistic approach to determine the local erosion of a watery debris flow. In Proceedings of the XI IAEG International Congress 2006, Liege, Belgium, 3–8 September 2006; p. S08-08.
64. Hussin, H.Y.; Quan Luna, B.; vanWesten, C.J.; Christen, M.; Malet, J.P.; van Asch Th, W.J. Parameterization of a numerical 2-D debris flow model with entrainment: A case study of the Faucon catchment, Southern French Alps. *Nat. Hazards Earth Syst. Sci.* **2012**, *12*, 3075–3090. [CrossRef]
65. Christen, M.; Kowalski, J.; Bartelt, P. RAMMS: Numerical simulation of dense snow avalanches in three-dimensional terrain. *Cold Reg. Sci. Technol.* **2010**, *63*, 1–14. [CrossRef]
66. Chung, T.J. *Computational Fluid Dynamics*, 4th ed.; Cambridge University Press: Cambridge, UK, 2006; p. 1012.
67. Li, S.M.; Liu, W.K. *Mesh Particle Methods*; Springer: Berlin/Heidelberg, Germany, 2007; p. 502. ISBN 978-3-540-22256-9.
68. George, P.L.; Borouchaki, H. *Delaunay Triangulation and Meshing, Application to Finite Elements*; Hermes: Paris, France, 1998; p. 416, ISBN 2-86601-692-0.
69. Gingold, R.A.; Monaghan, J.J. Smoothed particle hydrodynamics: Theory and application to non-spherical stars. *Mon. Not. R. Astr. Soc.* **1977**, *181*, 375–389. [CrossRef]
70. Pastor, M.; Haddad, B.; Sorbino, G.; Cuomo, S.; Drempetic, V. A depth integrated coupled SPH model for flow-like landslides and related phenomena. *Int. J. Numer. Anal. Methods Geomech.* **2009**, *33*, 143–172. [CrossRef]
71. Monaghan, J.J. SPH and Riemann solvers. *J. Comput. Phys.* **1997**, *136*, 298–307. [CrossRef]
72. Monaghan, J.J.; Kajtar, J.B. SPH particle boundary forces for arbitrary boundaries. *Comput. Phys. Commun.* **2009**, *180*, 1811–1820. [CrossRef]
73. Morris, J.P.; Fox, P.J.; Zhu, Y. Modeling low Reynolds number incompressible flows using SPH. *J. Comput. Phys.* **1997**, *136*, 214–226.
74. Oñate, E.; Idelsohn, S.R.; Del Pin, F.; Aubry, R. The particle finite element method. An overview. *Int. J. Comput. Methods* **2004**, *1*, 267–307. [CrossRef]
75. Idelsohn, S.R.; Oñate, E.; Del Pin, F. The particle finite element method: A powerful tool to solve incompressible flows with free-surfaces and breaking waves. *Int. J. Numer. Methods Eng.* **2004**, *61*, 964–989. [CrossRef]
76. Idelsohn, S.R.; Oñate, E.; Del Pin, F. A Lagrangian meshless finite element method applied to fuid–structure interaction problems. *Comput. Struct.* **2003**, *81*, 655–671. [CrossRef]
77. Codina, R. Pressure stability in fractional step finite element methods for incompressible flows. *J. Comput. Phys.* **2001**, *170*, 112–140. [CrossRef]

78. Belikov, V.; Semenov, A. Non-sibsonian interpolation on arbitrary system of points in Euclidean space and adaptive generatingisolines algorithm. Numerical Grid Generation in Computational Field Simulation. *Appl. Numer. Math.* **2000**, *32*, 371–387. [CrossRef]
79. Oñate, E. Derivation of stabilized equations for advective–diffusive transport and fluid flow problems. *Comput. Methods Appl. Mech. Eng.* **1998**, *151*, 233–267. [CrossRef]
80. Pasculli, A.; Minatti, L.; Audisio, C.; Sciarra, N. Insights on the application of some current SPH approaches for the study of muddy debris flow: Numerical and experimental comparison. Wit Transaction on Information and Communication Technologies. In Proceedings of the 10th International Conference on Advances in Fluid Mechanics, AFM 2014, A Coruna, Spain, 1–3 July 2014; Volume 82, pp. 3–14. [CrossRef]
81. Koshizuka, S.; Oka, Y. Moving particle semi-implicit method for fragmentation. *Nucl. Eng. Sci.* **1996**, *123*, 421–434. [CrossRef]
82. Mendez, F.J.; Mendez, M.A.; Sciarra, N.; Pasculli, A. Multi-objective analysis of the Sand Hypo-plasticity model calibration. *Acta Geotech.* **2024**, *19*, 4241–4254. [CrossRef]
83. Lei, D.; Zhang, Y.; Lu, Z.; Lin, H.; Fang, B.; Jiang, Z. Slope stability prediction using principal component analysis and hybrid machine learning approaches. *Appl. Sci.* **2024**, *14*, 6526. [CrossRef]

Disclaimer/Publisher's Note: The statements, opinions and data contained in all publications are solely those of the individual author(s) and contributor(s) and not of MDPI and/or the editor(s). MDPI and/or the editor(s) disclaim responsibility for any injury to people or property resulting from any ideas, methods, instructions or products referred to in the content.